EFFECT OF BUILD GEOMETRY AND BUILD PARAMETERS ON MICROSTRUCTURE, FATIGUE LIFE, AND TENSILE PROPERTIES OF ADDITIVELY MANUFACTURED ALLOY 718

A Thesis submitted in partial fulfillment of the

requirements for the degree of

Master of Science in Materials Science and Engineering

by

ANNA DUNN

B.S., Ohio University, 2020

2022

Wright State University

WRIGHT STATE UNIVERSITY

GRADUATE SCHOOL

07/14/2022

I HEREBY RECOMMEND THAT THE THESIS PREPARED UNDER MY SUPERVISION BY Anna Dunn ENTITLED Effect of Build Geometry and Build Parameters on Microstructure, Fatigue Life, and Tensile Properties of Additively Manufactured Alloy 718 BE ACCEPTED IN PARTIAL FULFILLMENT OF THE REQUIREMENTS FOR THE DEGREE OF Master of Science in Materials Science and Engineering

_____

Henry D, Young, Ph.D.
Thesis Co-Director

_____

Joy Gockel, Ph.D.
Thesis Co-Director

_____

Raghavan Srinivasan, Ph.D., P.E.
Chair, Mechanical and Materials Engineering Department

Committee on Final Examination:

_____

Henry D Young, Ph.D.

_____

Joy Gockel, Ph.D.

_____

Onome Scott-Emuakpor, Ph.D.

_____

Barry Milligan, Ph.D.
Dean of the Graduate Schoo1

ABSTRACT

Dunn, Anna. M.S.M.S.E., Department of Mechanical and Materials Engineering, Wright State University, 2022. Effect of Build Geometry and Build Parameters on Microstructure, Fatigue Life, and Tensile Properties of Additively Manufactured Alloy 718.

Additive Manufacturing (AM), particularly laser powder bed fusion, is being studied for use in critical component applications. Tensile and fatigue testing shows differences when built using different laser powers. However, when fabricated in an as-printed geometry, the gauge sections of the two specimens are different and experience different thermal behavior. This work explores microhardness, microstructure size, Niobium segregation, and porosity from samples made with varying laser power and different build geometry sizes representative of the gauge sections in the tensile and fatigue bars. Results show that microhardness varies spatially across the sample. Smaller diameter metallographic coupons (fatigue diameter) have a coarser microstructure and lower microhardness than the larger diameter (tensile diameter) when built using the same parameters. Therefore, the fatigue and tensile properties are not comparing the same material structure. Understanding the effect of build geometry on microstructure provides insight towards consistency in AM mechanical properties testing strategies.

Table of contents

List of Figures

List of Tables

1 Introduction

Additive manufacturing is a process that was first developed in 1980 by Beaman and Deckard who invented a method of additive manufacturing called selective laser sintering for plastics [1]. Additive Manufacturing is a process by which parts are built layer by layer. This manufacturing process allows for fast prototyping, low waste manufacturing, low-cost manufacturing, and can even produce parts that have a high accuracy to the CAD model. In general, additive manufacturing can be classified into two different types: direct and indirect processes. The direct process involves only one major step for the part fabrication process and the indirect process involves two major steps such as laser melting of a polymer binder and then sintering [2]. While there are a variety of materials that can now be produced via additive manufacturing, the maturity of each process for each material is different and dependent on the specific manufacturing process. For example, metals and ceramics are new to the process of additive manufacturing and still require a lot of research whereas polymeric additive manufacturing is relatively mature. This thesis focuses on direct additive manufacturing of metals, specifically Nickel Superalloy 718 via laser powder bed fusion, and provides a study on the effect of processing parameters and build geometry on microstructure, defects, tensile properties, and fatigue properties.

1.1 Additive manufacturing of metals

Additive manufacturing of metals is a relatively new process. There are three common additive technologies that are used for metals: Laser Powder Bed Fusion, Electron Beam Melting, and Direct Laser Metal Sintering. Each of these processes uses metal powder and a laser as a heat source to either melt or sinter the metal powder. Electron Beam Melting (EBM) is accomplished by heating a metal powder in a vacuum and using an electron beam to melt the powder layer by layer. This method produces parts with less residual stresses than other methods, but the surface roughness is usually worse compared to other AM methods. Both Laser Powder Bed Fusion and Direct Laser Metal Sintering are very similar. They both employ metal powder melted via a laser in a layer-by-layer fashion. However, the method used to produce the laser is different. Direct Laser Sintering uses optical lenses and Laser Powder Bed Fusion employs a system of drivers and mirrors [3]. These methods are commonly used in industry, but they introduce anisotropy and residual stresses due to cooling processes [4]. These issues can be rectified via post-fabrication heat treatment [3].

The specimens tested in this work were all produced via Laser Powder Bed Fusion and heat-treated for stress relief, retaining microstructure and defect structures. The defect microstructure and surface roughness all effect the mechanical properties of components. While this work primarily focuses on microstructure and other defects it is important to recognize that there are many factors that influence the performance of additive parts.

1.2 Motivation, applications, and contributions

Additive manufacturing is an important route to manufacturing of complex geometries. It also allows fabrication with materials that are difficult to work with [5]. This means that it's very important to improve and research additive manufacturing. The influence of processing parameters on defects and microstructure is particularly important, since these parameters strongly determine the mechanical properties of the material. Another potential influence on the microstructure is the build geometry. Working towards uncovering these relationships is important to improve the additive manufacturing process. Improving the additive process will improve applications for many different industries such as automotive, aerospace, and many others. Inconel 718 is often used in turbine blades for the aerospace industry and is historically hard to work with, thus improving the additive processes for such a material would greatly benefit the aerospace industry [5].

This work focuses on studying the processing parameters and effect of build geometry for additively manufactured Alloy 718 using laser powder bed fusion. Through experimentation, this work contributes to the knowledge about additively manufactured Alloy 718. First, this work confirms the existence of spatial variation in microhardness in LBPF Alloy 718 parts. Second, it determines that increasing bulk laser powers increases grain sizes and Nb segregation through qualitative microstructural analysis and Microhardness testing, resulting in changes in mechanical properties. Third, it suggests that changing the build geometry while using the same processing parameters results in changes in grain sizes and Nb segregation through qualitative microstructural analysis and microhardness testing.

2 Background and literature review

A detailed literature review was conducted in order to understand how the build parameters could affect fatigue life and tensile properties, as well as how the build geometry effects the microstructure.

2.1 Laser powder bed fusion

Laser powder bed fusion is one of the common methods for fabricating metal parts [3]. This process involves the spreading of a layer of powder across a substrate and then selectively melting appropriate regions using a laser beam with a high local power. The part is then lowered by one layer thickness and more powder is spread across the “build plate”. This cycle repeats itself until the last layer is melted and solidified. Figure 1 shows a schematic of the Laser Powder Bed Fusion process [4].

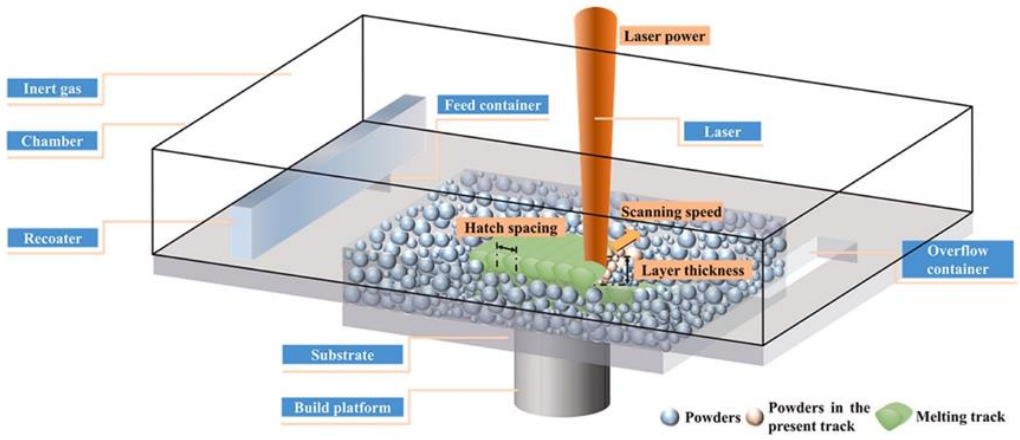

Figure 1: typical schematic of the Laser Powder Bed Fusion process. The words in white show machine components while the words in black show processing parameters [4].

This figure also illustrates which processing parameters are important. Processing parameters play a huge role in the success or failure of part fabrication and play critical roles in the formation of surface roughness, residual stress, and porosity. LPBF is a complex process that involves energy absorption, heat transfer, phases changes, fluid flow, and even chemical reactions. All these processes are influenced by the processing parameters and effect the defects and microstructure of the fabricated part [4].

The interaction between the powder and the laser determines the amount of heat absorbed by the powder. This can be changed by optimizing laser characteristics and the reflectivity of the powder. While the laser characteristics can be machine specific, the scanning speed and laser power, along with the layer thickness, can be changed and optimized to achieve the desired microstructure or to reduce defects [4]. However, changing these parameters can also effect surface roughness, melt pool size, viscosity,

cooling rate and even cause balling or keyhole mode cooling, which can have detrimental effects on the porosity of the finished part [4,6].

Laser powder bed fusion has many important aspects such as amount of heat absorbed, heat transfer a crossed phases and the material, and the fluid flow characteristics of the melt pool. The heat absorbed by the system depends on the material properties and the powder characteristics such as particle size and density [6]. LPBF results in thermal cycles that vary based on location which means that the microstructure and properties of AM parts are inhomogeneous. This is very similar to welding since the moving heat source results in localized thermal cycling. However, AM is different in that the interaction between neighboring metal particles and the previous solidified layer all interact with the heat source as well. This means that there are multiple thermal cycles seen by the powder material and by previously solidified build layers, all of which contribute to the inhomogeneity of the microstructure and defects in AM parts [6].

Since thermal cycling during LPBF is complex, a basic understanding of heat transfer and phase transformations in alloys is helpful. Phase transformation and heat transfer are both driven by a tendency to reach equilibrium. While pressure does play a part in phase transformation and equilibrium, the primary component in AM processes that dominates equilibrium considerations is temperature. Due to the heat produced locally by the laser, small regions of the material absorb enough energy to change phase. The solid particles liquify near the laser and create a melt pool which then rapidly solidifies as the laser moves away from the affected area. This rapid solidification is driven the decrease in Gibbs free energy due to undercooling [7]. This not only

contributes to the inhomogeneity of microstructure and defects in AM parts but also causes residual stresses that must be addressed as well [3, 4, 6, 7, 8].

LPBF is a complex process that depends on material properties, powder characteristics, processing parameters, heat transfer and the phase changes involved, [6, 7]. While the basic principles for Laser Powder Bed Fusion are the same for all types of materials, material behavior can vary significantly during the process. Metals and alloys in general need high power lasers for successful LPBF. However, alloys may have issues with vaporization of alloying elements with lower boiling points than the base metal or vice versa [8]. This means that individual alloys behave differently during this process. This thesis focuses on LPBF of Alloy 718, so a detailed discussion of Nickel Superalloys, Alloy 718, and the general trends seen for LPBF-produced Alloy 718 should also be discussed.

2.2 Nickel super alloys

Superalloys are metallic alloys that can be used at high temperatures. These alloys are oxidation and creep resistant at temperatures upward of 0.7 T_m. Typically, they are alloys of nickel, iron, or cobalt [9]. Most nickel superalloys are alloyed with aluminum and titanium for high strength applications, such as in turbine disks. Niobium is used to create a precipitate phase (Ɣ'') [9]. Both the phases created by adding aluminum and titanium and the secondary phase created by adding niobium aid in strengthening the material both at higher and lower temperatures. Typically, metals lose their strength as temperature increases. However, this is not the case for superalloys due to their alloying effects. The aluminum and titanium are used to strengthen nickel at high temperatures by introducing cross slipping of dislocations on {100} planes. This locks the dislocations,

causing a strengthening effect at elevated temperatures [9]. Nickel and their subsequent alloys typically have an FCC crystal structure however, some alloying elements such as niobium may change the crystal structure for the phases they inhabit. [9]

2.2.1 Structure and properties of Alloy 718

Alloy 718 is not a new alloy. It was first developed in the 1950s and is strengthened by the phase ϒ'' phase [10]. It consists of 50-55wt% Ni, 17-21wt% Cr, 4.8-5.5wt% Nb, 2.8-3wt% Mo, 0.65-1.15wt% Ti, and 1wt% Cr [11] . Alloy 718 has many different phases, not all have the same crystal structure. There are two FCC phases called the ϒ and ϒ' phase. Niobium is added to harden this alloy at lower temperatures to insure sufficient mechanical properties both at high temperatures and lower temperatures which creates other phases in alloy 718. Unlike the previously mentioned phases in Alloy 718 the ϒ'' phases have a tetragonal ordered body-center crystal structure. This structure has lattice parameters that are different from the lattice parameters of the other phases which increases lattice distortion therefore increasing strength. This phase has lattice parameters of a=0.362nm=b, C=0.741nm [9,10]. The following images are representations of the lattice structures present in Alloy 718.

Figure 2: unit cells representing (a) the Y phase and (b) the Y' phase [9].

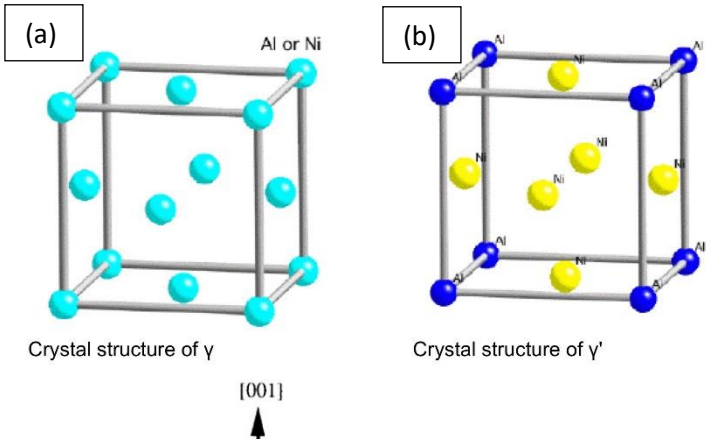

Figure 3: unit cell of Y'' phase in INCONEL 718 [10].

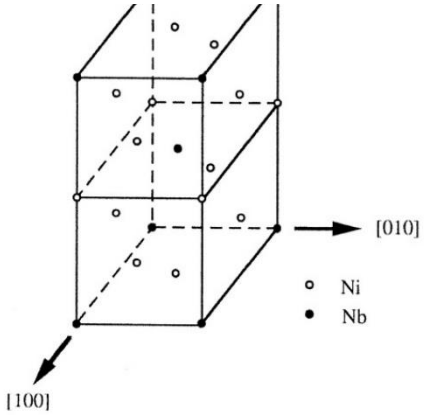

While these are the main phases in Alloy 718, there are also precipitates such as close packed hexagonal laves phases, orthorhombic δ phases, and tetragonal σ phases [11]. All of these phases are generally considered undesired as they are brittle phases that may increase the strength of Alloy 718 but also decreases its ductility [11, 12].

The properties of Alloy 718 are dependent on how the material is manufactured, and AM Alloy 718 can be very different than traditionally fabricated Alloy 718. In general for heat treated wrought alloy 718, the ultimate tensile strength is 199ksi at room temperature and 160Ksi at elevated temperatures; the yield strength is 160Ksi at room temperature and 142Ksi at elevated temperatures; and the elongation to fracture is 25% for room temperature and 18% at elevated temperatures [12].

2.3 Laser powder bed fusion for Alloy 718

AM parts including parts produced via laser powder bed fusion can have many advantages, but they can also be limited when compared to their traditionally made counter parts. Their quality, prediction of their mechanical properties, and reproducibility can be low. All of these issues are linked to porosity, microstructural defects and anisotropy, and general microstructural heterogeneity [11].

The grain structure of additive 718 tends to be elongated along the build direction, usually denoted as z and is equiaxed in the scanning surface, or XY plane. This structure is formed via elongated columnar dendrites that solidify after the heat source is removed. These grains also extend through multiple build layers due to re-melting and re-solidification [11]. It should also be noted that the build parameters also effect the microstructure seen in AM Alloy 718. One study showed that higher laser powers with moderate scanning speeds produce relatively larger grains with characteristic crystallographic lamellar microstructures. Lower laser powers and higher scanning speeds tend to produce much smaller polycrystalline microstructures [13]. Porosity is also another important defect feature in AM. Typically the types of pores seen are spherical pores caused by dissolved gas within the melt pool, large spherical pores called

key-hole pores caused by vaporization of material and the subsequent collapse of the vapor cavity, and irregularly shaped pores known as lack-of-fusion pores which stem from incomplete melting of powder particles [11].

The tensile properties of AM Inconel 718 very greatly depending on the post processing of the material. In general, 718 is heat treated after being manufactured. resulting in higher strengths and lower ductilities. This is due to the formation of precipitate hardening phases ϒ’ and ϒ’’ during heat treatment which increase alloy strength [11]. This is important to note regarding this study, since the specimens in this thesis are as built. In general, the strength of AM parts, whether heat treated or not, are higher than cast 718 but lower than wrought 718 [11]. This is because the grain structure of AM 718 is finer than cast 718 [14] and the porosity of AM parts tends to be higher than wrought parts [15]. However, due to the complex thermal cycling in AM parts, typically finer microstructure, and presences of hard laves phase inclusions may contribute to strengthening [11] and [16].

The hardness of AM 718 also tends to vary spatially, due to porosity and inhomogeneous microstructure, and often depends on the method of AM manufacturing and specific processing parameters [11]. Some studies have shown that the hardness of AM 718 decreases with increasing build height, while others report that such variation is negligible [17, 18]. Studies have also shown that there is no significant difference between average microhardness in planes parallel and perpendicular to the build direction, for both as-built and heat-treated AM 718 [17, 18]. However, studies by Lesko C. and Babu et al. have shown that there is a difference in microhardness within the planes themselves in both the perpendicular plane and the parallel plane, with higher

values in HV being closer to the build plate in the parallel and the center of the plane in the perpendicular direction [16, 19]. Both works also noted the differences in microhardness in relation to laser powers used during the AM process [16, 19].

The mechanical properties of AM Inconel as-built parts can be inferior to their wrought or cast counterparts. In general, the fatigue limits were significantly lower for AM Inconel 718 due to surface roughness, microstructural defects, and porosity [11]. Residual stresses can also play a factor in reducing the fatigue life [11].

2.4 Fatigue

To understand the relationship between the bulk laser power and the fatigue life presented in this work a detailed discussion must be conducted on fatigue. Fatigue is damage done to a material due to repeated use. This is due to cyclic like loading seen by the component throughout its lifetime. This induces stresses within the material that cause damage such as cracks which are initiated by defects. While fatigue can be caused by repeated loading on the material it can also be caused by other modes, such as thermal expansion, corrosion, or vibration. If a process causes stress accumulation within the material that leads to deformations it contributes to fatigue. Aside from high cycle fatigue and low cycle fatigue there is also creep fatigue, thermo-fatigue, corrosion fatigue, and creep accelerated by vibration [20]. Once the fatigue life of a material has been met the material usually fractures. This can depend heavily on the external environment and in the case of metals a higher external temperature yields ductile fractures, and a lower external pressure yields brittle fractures [20].

Fatigue can be classified as two different types: Low Cycle Fatigue and High Cycle Fatigue. Low Cycle Fatigue is characterized by its lower number of cycles (typically 10^4

or less) and by the existence of plastic deformation within the fatigue cycle. The plastic deformation during the cycle can sometimes lead to work hardening and or softening [20, 21]. Low Cycle Fatigue consists of loading in tension until plastic deformation starts at the yield point and then loading in compression until the yield point again. High Cycle Fatigue on the other hand typically consists of many more cycles than low cycle fatigue. High Cycle Fatigue also consists of only elastic deformation [21].

Fatigue occurs in stages that can be seen in most materials. The duration of each stage or lack thereof is dependent upon the mechanical properties of the material. In the first step, damage accumulates in the microstructure [20, 21]. This consists of microcracks which are strong stress concentrators. In the second stage, the cracks grow until they are stopped by precipitates, dislocations, or other obstacles. The depth of these cracks is very small compared to the cross section of the material and they are typically several grain sizes in length, and they are called small cracks [20, 21]. In the third stage, the small cracks push through the various obstacles and grow to become long cracks, which are strong stress concentrators. Finally, in the fourth stage, the material fractures [20]. Something to note is that the first two stages may not be present if the material contains crack like defects such as porosity and lack of fusion pores often found in AM materials [20].

There are many factors that affect fatigue life in materials. Some of the most common ones are surface roughness, frequency of loading, residual stress and strain, stress concentration, temperature, loading history, and environmental conditions [20]. One of the most important factors in fatigue is that materials subjected to the same loading and same environments may not fail at the same number of cycles [21]. This is

because of the defects and microstructural differences within a material. Typically, this is shown by statistical scatter in experimental results. The results however are typically dependent on the size of the part undergoing fatigue. One of the most important factors is surface roughness. This is because most of the stress is concentrated at the surface, thus a rough surface provides many cracks initiation sites when the stress is concentrated on the surface [21].

2.4.1 Fatigue in additive materials

Fatigue is common for all materials especially metals, however it is particularly important for additive materials. Additive materials tend to have defects in microstructure, porosity, and surface roughness that effect fatigue life [11]. S. Shao and N. Shamsaei proposed models to describe the synergistic effects defects and the microstructure on the fatigue behavior of laser powder bed fusion metal materials [22]. This is because AM parts tend to have a shorter fatigue life and a lower fatigue limit than parts made via other manufacturing methods. This is due to the defects, such as gas pores and lack of fusion pores, anisotropy, and their sensitivity to the build parameters. One such model proposed by this research group is called the Murakami's defect sensitive fatigue (DSF) model. This model assumes that all defects are similar enough to cracks so they can be treated as cracks within the model. However, this model does not take into account microstructural or defect shape [22]. When taking into account the shape of the pores a Linear elastic-finite element calculation can be used to change the two characteristic diameters of the pore to match the shape. This method can better asses the stress intensity of the crack initiation at the pores. The combination of these two methods

in junction with the Murakami's DSF model has been found to give a better correlation between the fatigue data and the defects and microstructure [22].

Another study done on AM titanium discussed the effect of stress porosity and crystallographic texture of fatigue. This was done using LPBF titanium specimens that were machined to remove the contour layers. The specimens were then subjected to high cycle fatigue testing to determine their failure properties and their fatigue crack growth rates [23]. Upon inspection of the material during this experiment it is clear that the specimens that were not Hot isostatically pressed (HIP)showed crack initiation at the lack of fusion pores and that the HIP specimens showed crack initiation within the grain structure of the material. A brief characterization of the microstructure was also conducted, and it was concluded that the scan length during the AM process influences the texture of the microstructure [23]. By analyzing the texture of the grains using EBSD it can be concluded that the texture does not affect the fatigue crack growth rate. However, the crystallographic texture does have an effect on the yield strength and the fracture toughness [23].

2.4.2 Fatigue in Alloy 718

Now that fatigue in general and fatigue in additive metal components have been discussed a more detailed discussion of fatigue in additively manufactured Inconel 718 is necessary. One such paper by Balachandramurthi et al. discusses the correlation between microstructure and crack growth in 718 [24]. This study employed two different AM methods: Electron Beam Melting (EBM) and laser powder bed fusion. Specimens made via both AM processes were either solution treated, HIP and aged (STA condition) or

brought to STA condition without being HIP. These samples were tested using a 4-point bending method until cracking occurred in the specimens [24]. This method creates a situation where solely bending stress is applied to the sample. The specimens in this work were tested using axial fatigue instead of the 4-point bending method, which is different than stress that causes bending fatigue. Axial fatigue is caused by applying an axial load and inducing axial stress to the sample. Both induce normal stress within the material however they cause the material to deform in different ways. During bending, materials will deform due to compression along the top of the sample and tension along the bottom of the material. During axial loading the sample will deform along the axis where the loads are applied in only either tension or compression [21].

The following image shows the method of fatigue crack propagation within the samples tested.

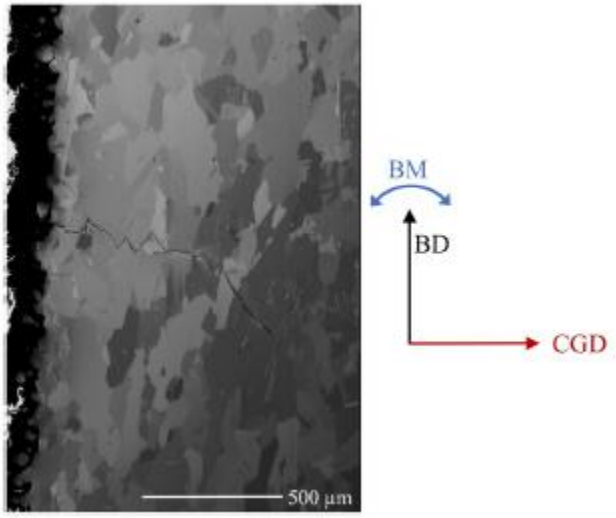

Figure 4: A BSE image of the crack path through the LPBF HIP + STA sample where BD is the build direction, CGD is the crack growth direction, and BM is the bending moment [24].

This image shows the transgranular method of crack propagation through the 718 samples. The figure above shows the plan parallel to the build direction. Since the microstructure of AM parts an anisotropy and the grains tend to be elongated along the build direction The results from this study indicate that the fatigue crack propagation also depends on the direction of the loading with respect to the build direction [24].

As discussed, fatigue is a multi-faceted issue especially for additive parts thus it is important to discuss how the processing parameters effect the fatigue life of additively manufactured Inconel 718. One such study preformed a test on the fatigue life of Inconel 718 with different processing parameters found that processing parameters the tend to produce significant porosity significantly reduce the fatigue life [25]. This study explored laser power, hatch spacing, and laser speed. These samples were machined to reduce the influence of surface roughness [25].

Another study by Sheridan, L discussed the effect of processing parameters on porosity and fatigue life only two bulk laser powers were used 285W and 370W but multiple scanning speeds, hatch spacings, and scanning strategies were used [26]. During the study that used the highest bulk laser power the specimens were produced with an average density of 99.9% however the size of the pores seen were different based on the scanning strategy. These specimens also had spherical gas porosity which indicates that the bulk power used caused over melting [26]. This study showed that scanning strategies that produce pores with smaller diameters have longer fatigue lives than scanning strategies that produce pores with larger diameters [26]. In the second study that used the lowest bulk laser power showed significantly lower porosity with samples with the

narrowest hatch spacing and higher scanning speeds which lead to higher fatigue lives [26].

These works show that processing parameters for AM processing determine the microstructure seen, porosity and mechanical properties however it does not go into detail on the effect of bulk laser power. This is discussed further later in this work.

2.5 Tensile test

Some of the most basic mechanical properties of a material can be obtained through a tension test. This is very important for Additive Materials because the manufacturing process is relatively new, so the process is not necessarily optimized or studied enough to produce consistent parts with properties like their conventionally made counter parts. Tensile tests in general are tests where specimens with a specific geometry are pulled apart using an increasing axial load. The data collected during the tensile test are axial displacement, force, and if an extensometer is used strain. The data is then represented using the following equations [27]:

1) $$\sigma = \frac{P}{A}$$

2) $$\varepsilon = \frac{L - L_o}{L_o}$$

This is then plotted as an Engineering stress strain curve. This graph can give properties of the material such as the yield strength, or the stress that begins to produce permanent deformation, the ultimate yield strength, or the maximum stress, and the elongation to failure, or the amount the material stretches before it fractures [27].

While the tensile properties of many traditionally made materials are well known the tensile properties of additive materials are still being studied thus, a discussion of the tensile properties of additively manufactured materials is necessary.

2.5.1 Tensile properties of additive materials

Before looking into the tensile properties of Alloy 718, a general discussion of the effects of AM on tensile properties should be discussed. One such study determined that when producing Maraging steel with laser powder bed fusion determined that the yield strength and the ultimate tensile stress are consistently higher than wrought maraging steel. Upon analysis of the microstructure of these tensile bar precipitates and other inclusions were found that are not normally found in the wrought materials due to the complex thermal interactions when using laser powder bed fusion and could attribute to the increase in strength. The ductility however was noted to be significantly lower [28].

Another study on Ti-6Al-4V discussed the effect of surface roughness introduced through the AM process on tensile properties. This study was conducted by testing AM Ti-6Al-4V bars that were left as built and bars that were machined to reduce the surface roughness. This study found that while the ultimate yield strength was not significantly impacted by the surface roughness the yield strength was decreased by 12.2% [29]. The elongation of the machined bars was increased by 24.9% and the unmachined bars did not behave significantly differently in the first elastic stage and the start of plastic deformation than the simulation used to predict the tensile behavior but does differ during the end stages and during failure [29].

2.5.2 Tensile properties of additively manufactured Alloy 718

The tensile properties of AM Alloy 718 have been studied by many. But their strength and ductility depend on the microstructure and defects such as porosity. In general, for AM Alloy 718 the strength is lower than its traditionally made counter parts, but its ductility is higher [11]. Parts produced through laser powder bed fusion however usually have higher strength than cast Alloy 718 but lower strength than wrought Inconel 718 this is usually attributed to the finer microstructure and lower alloying element segregation [11]. Studies have also shown that the anisotropy induced through the process increases the ductility of samples tested along the build direction [30].

One of the main contributing factors to the ductility of AM 718 is the porosity [11]. However, in some studies there is very little change in both strength and ductility depending on the processing parameters [25]. The only processing parameters in these studies that produced significant changes in ductility are processing parameters that specifically result in an increase in porosity indicating that this is a very important factor in producing ductile parts [25].

While porosity is an important contributing factor in the ductility of AM Alloy 718 some studies have shown that Laser powder bed fusion may have an impact on the strengthening precipitates found in Alloy 718, one study compared the tensile properties of as built AM specimens and wrought specimens. This study reported that 718 specimens built with laser powers of 260W, 320W and 340W all resulted in tensile specimens with a 15% increase in yield stress when compared to wrought Alloy 718 which has been attributed to the inclusion of nanosized precipitate particles that anchor dislocations leading to an increase in strength [31].

3 Mechanical testing:

The first tests run in this experiment were tensile and fatigue tests designed to assess the mechanical properties of as built Alloy 718 samples built with various bulk laser powers. The following sections discuss the mechanical testing conducted on these samples, the results of this testing, and the resulting conclusions for the mechanical testing.

3.1 Methods:

3.1.1 Specimen Geometry

The specimens were built in a vertical orientation and were pulled along the build direction. Which is defined below with the following schematic.

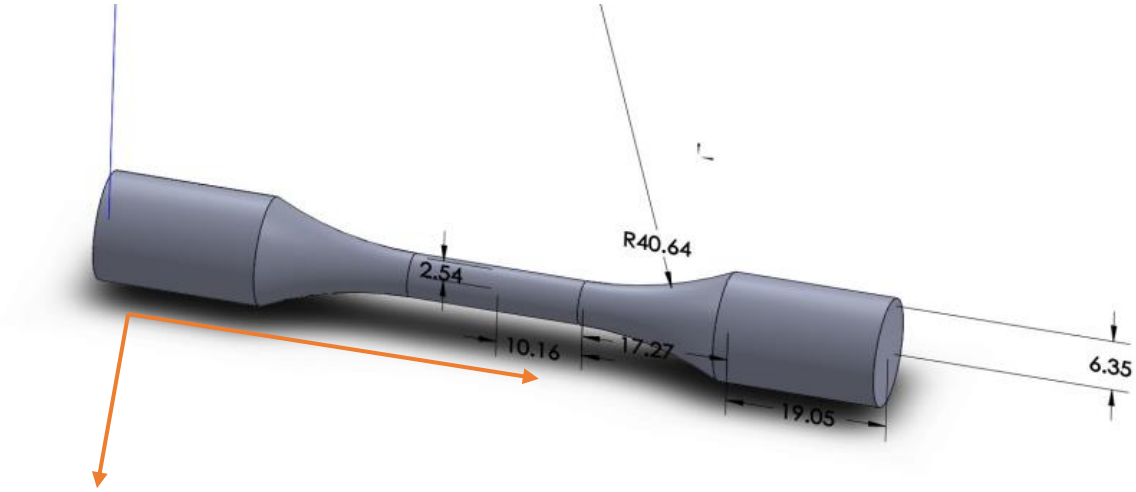

Figure 5: schematic of tensile bars used in this test with dimensions in mm and build direction defined with arrows as BD

The specimens for the fatigue testing were built in a vertical orientation and fatigued along the build direction. The following schematic defines the build direction.

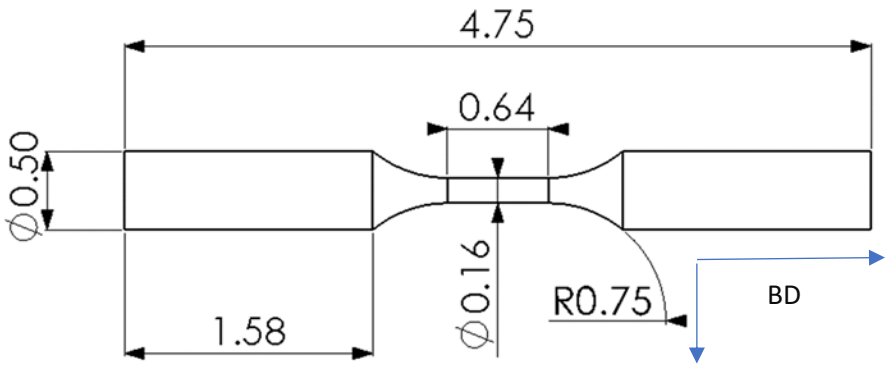

Figure 6: schematic of fatigue samples with dimensions in inches and build direction defined as BD by arrows.

3.1.2 Additive manufacturing build

The test bars were built using an Open Additive Panda PBF-LB machine. These bars were fabricated with the same contour processing parameters, same hatch spacing, same layer thickness, and same bulk laser speed. The bulk laser power, however, was varied for this experiment. The following table shows the bulk power parameters used for the tensile and fatigue specimens. The following values are the parameters used for the tensile bars: Bulk Laser speed 800mm/s, a contour laser speed of 560mm/s, hatch spacing of 70µm, a layer thickness of 30µm, and a contour power of 150W.

Table 1:Table of tensile bar build parameters, Bulk laser power.

Sample Number	Bulk Laser Power (W)
1	230W
2	230W
3	230W
4	280W
5	280W
6	280W
7	330W
8	330W
9	330W

Table 2: table of build parameters for each fatigue bar and their specimen number.

Specimen No	Contour Power (W)	Contour Speed (mm/s)	Bulk Power (W)	Bulk Speed (mm/s)
9_0	150	560	230	800
9_1	150	560	230	800
9_2	150	560	230	800
25	150	560	280	800
26	150	560	280	800
27	150	560	280	800
28	150	560	330	800
29	150	560	330	800
30	150	560	330	800

3.1.3 Tensile testing

The tensile testing was done using an MTS Servo hydraulic load frame and the tensile specimens as described in section 3.1.1. The specimens are fixed into the load frame via grips in the heads and then an 0.577'' GL extensometer is attached to the specimen. This test was run in displacement control and with a displacement of 1in/1000sec. Typically a tensile test is run with a standardized program and the extensometer is removed before the sample breaks in order to keep the extensometer from becoming damaged [32, 33]. The tensile testing was conducted by Dino Celli at the

Turbine Engine Fatigue Facility (TEFF) within the Air Force Research Laboratory (AFRL).

3.1.4 Fatigue Testing

The fatigue test was set up to avoid buckling of the fatigue bar by using an R value of 0.1. This resulted in an axial tension fatigue test run at a stress of 100 KSI or 690 Mpa. All bars were tested at room temperature at AFRL using the fatigue testing machine at the TEFF. Testing was performed collaboratively with Rachel Evans.

For the fatigue testing, the specimens were tested on an MTS Servo-Hydraulic Load Frame using the station manager multipurpose test square program. First, the diameter of the gage section is measured for each test bar three times, getting an average cross-sectional area for each bar. Next, the machine is set to manual control and ensured that it is in displacement mode. Then the moving head is zeroed [32]. Next the program was switched to force control under manual control and the force was zeroed. The specimen must be loaded in displacement control. The specimen was loaded into the bottom moving head, ensuring that the specimen has about a ¼ in of the grip section exposed. Next, the grip pressure is raised on the bottom head to 2000 psi. The computer is used to raise the bottom head until the top grip section of the sample is in the top head leave about ¼ in of the grip section of the sample exposed and the grip is closed. The extensometer is placed onto the specimen's gage section. The extensometer must be both level and centered before the pin is removed.

The computer is used to offset the current readings. A procedure was created for the fatigue test using a cyclic loading, Sine tempered setting and imputing the minimum and maximum force used in the test. These values were found by multiplying the chosen

stress of 100Ksi by the cross-sectional area for the maximum force and then multiplying that R value of 0.1 to get the minimum force. The interlocks were set to 0.05 for displacement control before manual control is disabled and the test is run [32]. The specimens were removed when the loop on the graph starts to become unstable. The extensometer was removed, and the test resumed until the specimen breaks.

3.1.5 Fractography

All samples were cut using a Buehler Isomet 5000 Linear Precession saw to remove the grip section from the gauge section containing the fracture surface. This was done so that the fracture surfaces can fit inside the SEM where they were then imaged at various magnifications to get an understanding of the features present.

3.2 Results

The following sections discuss the results from the Mechanical testing including the Stress strain curves developed from the tensile testing, fractography for both tensile and fatigue testing, strength and ductility data extracted from the stress strain curve, and cycles to failure for fatigue testing.

3.2.1 Tensile Testing

This section focuses on the results from the tensile testing. Below is the graph generated in MATLAB from the tensile data for all 9 specimens.

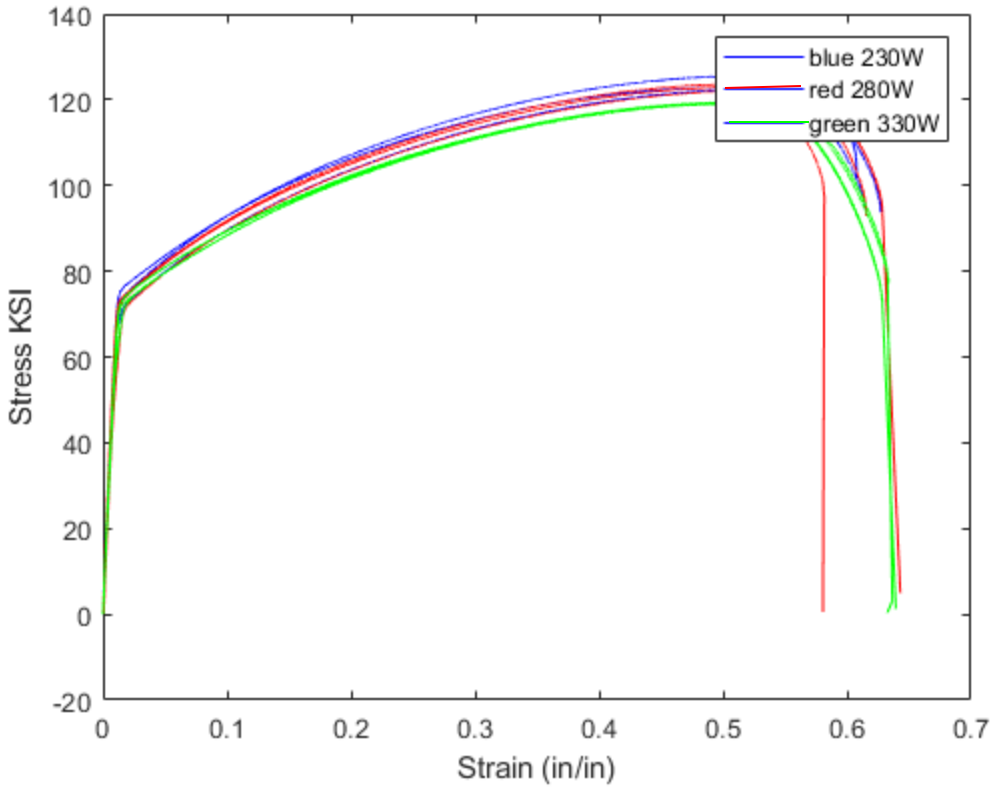

Figure 7: Stress Stain curve for samples fabricated with 230 W, 280 W and 330 W.

Below is the Table of strength and ductility data pulled from the above stress strain curve. Here the bulk power used appears to have little effect on the yield strength of the samples, since there doesn't appear to be an apparent trend. The yield strengths do, however, have a standard deviation of 2.5 indicating that they are statistically different from each other. The ultimate tensile strengths, however, appear to have lower strengths for higher powers indicating that the laser power influences strain hardening rates which increases the ultimate yield strength. The ductility of these samples is essentially the same for all three powers. The elongation to failure has a standard deviation of 0.033 indicating that they are not statistically different from one another.

There is one sample with a lower elongation to failure than the other which is most likely due to porosity.

Table 3: Table of yield strength, ultimate tensile strength, and elongation for tensile specimens.

specimen bulk laser power	**yield strength (Ksi)**	**Ultimate Yield strength (Ksi)**	**Elongation to Failure (in/in)**
230	75	126	0.62
230	71	127	0.61
230	68	123	0.627
280	73	126	0.582
280	68	125	0.62
280	69	125	0.643
330	68	119	0.652
330	71	120	0.68
330	72	119	0.682

3.2.1.1 Tensile Testing Fractography

The following images give the fractography taken of the fracture surfaces for the tensile samples.

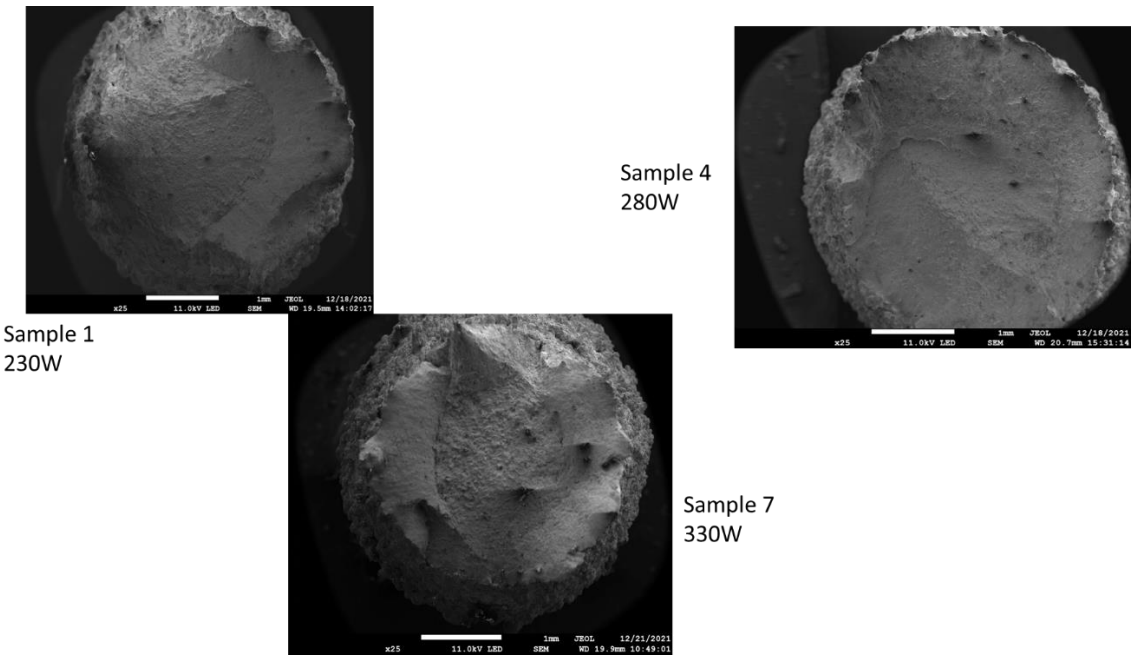

Figure 8: Fractography images from tensile testing

Here all images have the cup and cone shape typical of ductile tensile specimens however the sample built with 280W is not as pronounced, this is due to higher porosity within the sample which was uncovered using fractography using the SEM seen in the following figure.

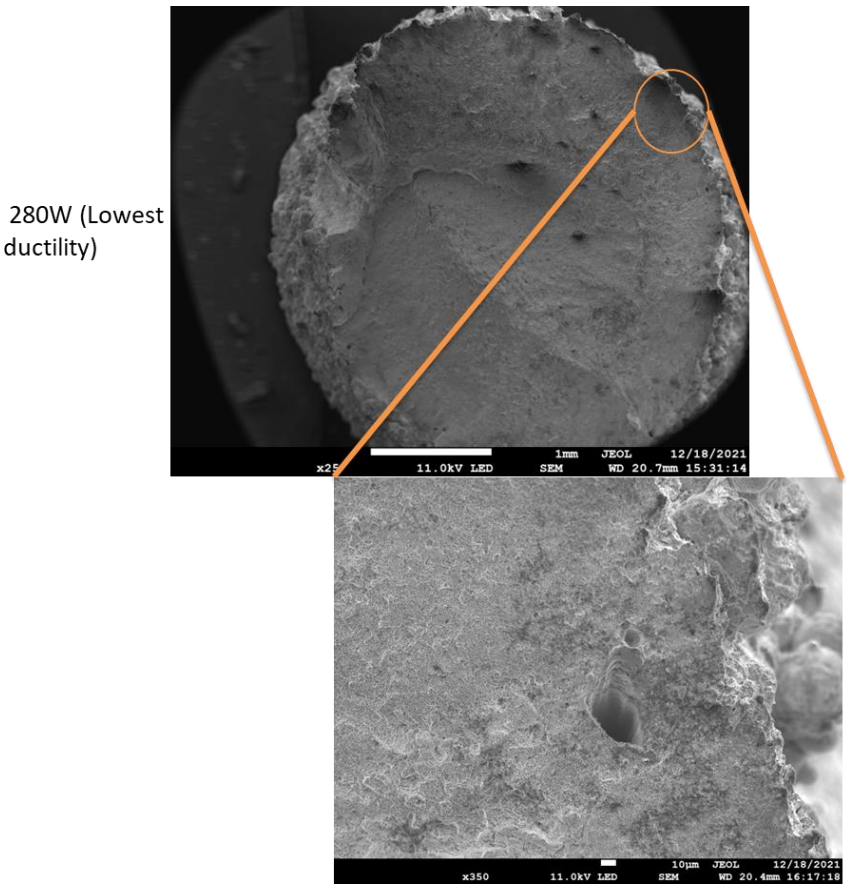

Figure 9: Fractography image of tensile sample with lowest ductility featuring example of porosity seen with in the sample.

3.2.2 Fatigue testing

The following sections give the results from the fatigue tests for 9 samples fabricated with 230W, 280W, and 330W.

3.2.2.1 Fatigue cycles to failure

This section focuses on the fatigue life of the samples in this study. Below is a table giving the bulk laser power and the cycles to failure.

Table 4: table showing the bulk power compared to the cycles to failure for

Specimen No	Bulk Power (W)	Cycles to Failure
9_0	230	22669
9_1	230	26490
9_2	230	21536
25	280	20839
26	280	21517
27	280	14073
28	330	15818
29	330	17000
30	330	20224

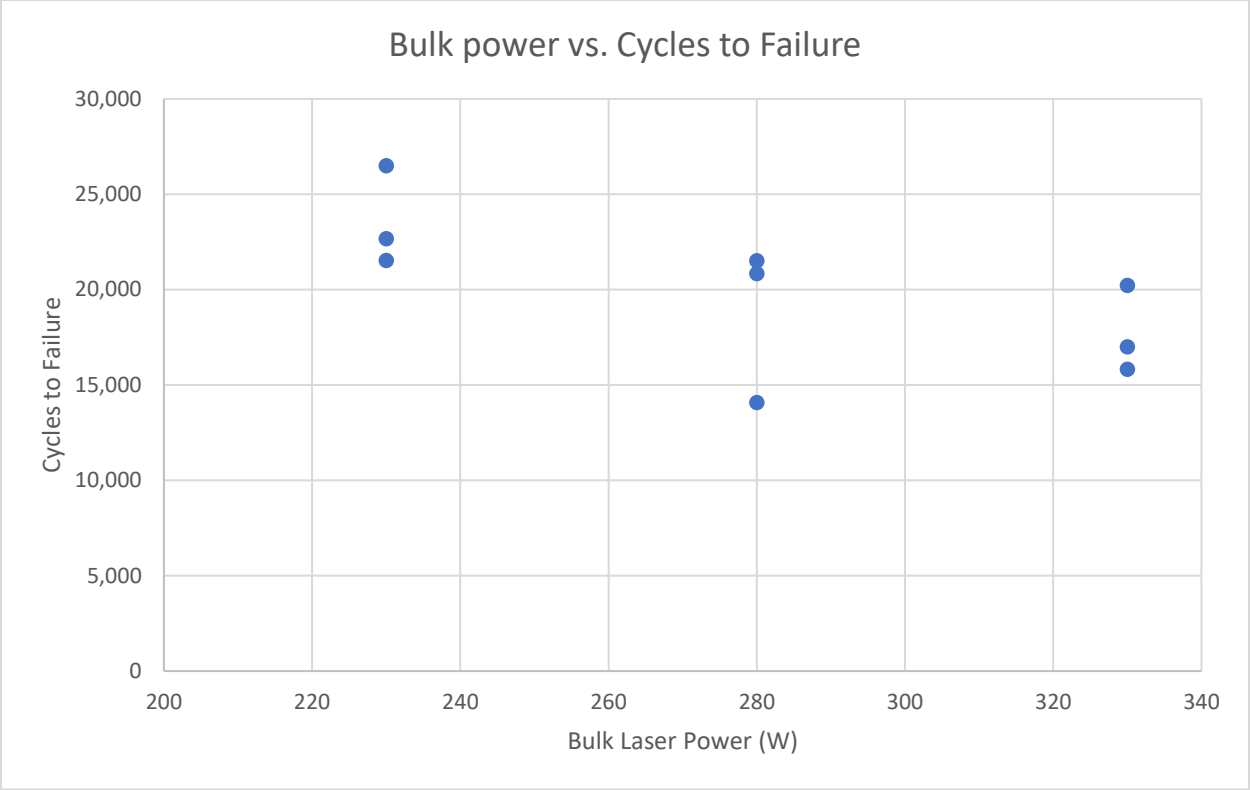

Figure 10: Graph of the cycles to failure vs. the bulk laser power.

The figure above shows the relationship between bulk laser power and the cycles to failure. Here, in general the cycles to failure decreases as the bulk power increases. This can be due to a variety of things including a change in grain size, porosity, and surface roughness for samples built with different processing parameters. While this study does not discuss surface roughness in detail it is an important aspect of fatigue that can be explored in future works. This work focuses on Microstructural defects and a limited study on porosity to explain the results from the mechanical properties seen here.

3.2.2.2 Fatigue Testing Fractography

The following figures give the fractography images take of the fatigue specimens along with areas of importance within the fracture surfaces that can explore the fatigue behavior.

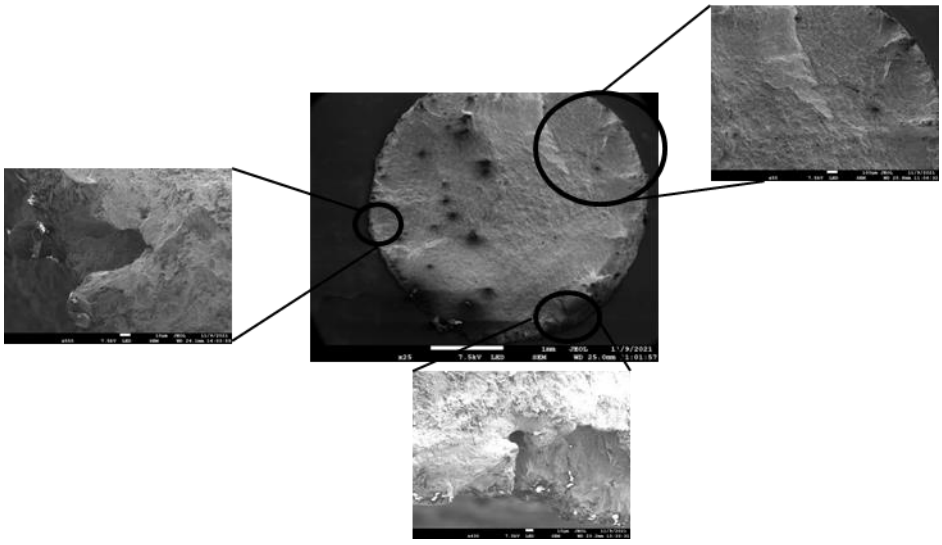

Figure 11: Figure 3: Fractography images for a fatigue sample built with 230W

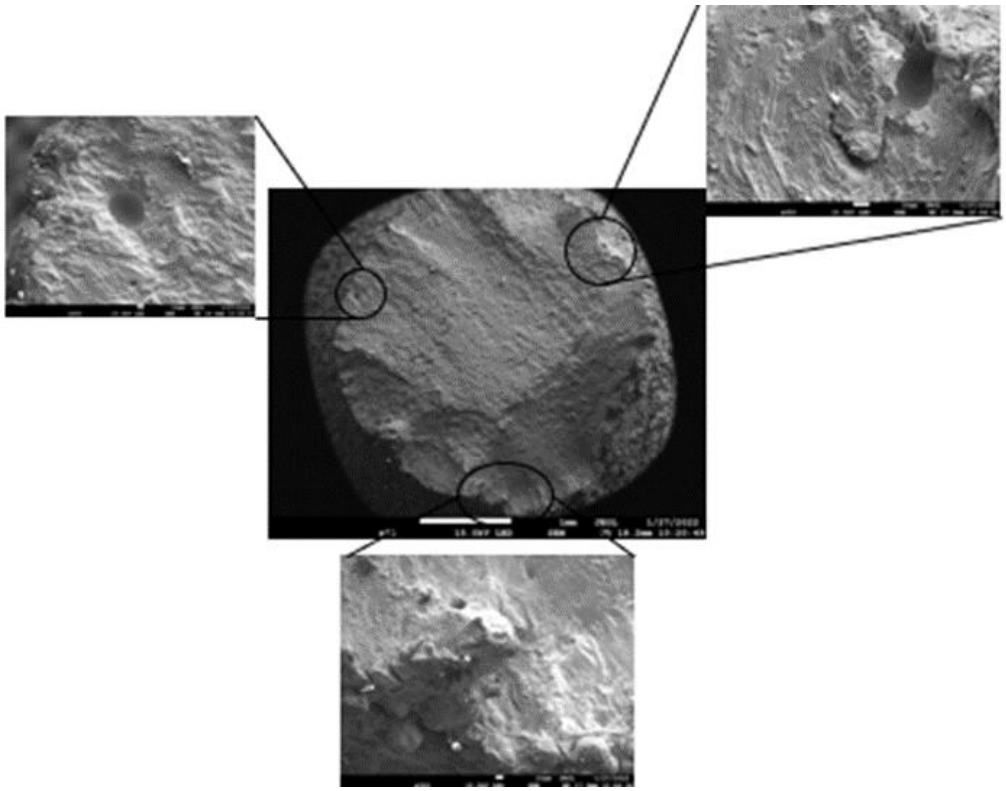

Figure 12: fractography images for 280 W sample.

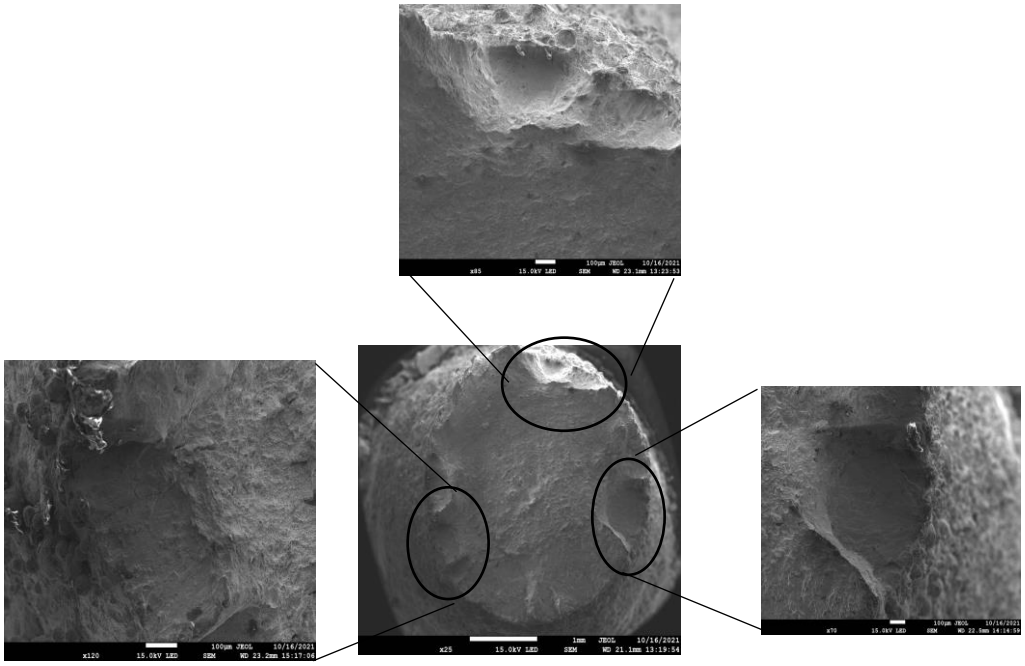

Figure 2: Fractography images for a fatigue sample build with 330W

Above in both images the surfaces are clearly rough however there are indications of larger surface notches, sub surface pores and other defects contributing to the lower fatigue life in samples built with 330W than there are in 230W. These features can contribute to a decrease in fatigue life; however, the surface roughness and porosity is only one aspect of the defects that affect fatigue life. In general, the grains in samples made with lower bulk laser powers tend to have finer grains than samples made with higher powers, which can influence crack propagation. The following sections in this work discuss materials characterization of representative samples for the gauge section for both the fatigue samples and the tensile samples. This was done to determine what

microstructural aspects effect the mechanical properties discussed above and to determine if the tensile properties and fatigue properties of AM 718 is comparable.

3.3 Conclusions

In the sections above the tensile properties and fatigue properties are discussed. In, general the cycles to failure for the fatigue specimens tend to decrease as the bulk power increases, the ultimate tensile strength also tends to decrease as the bulk power increases. However, the yield strength does not appear to be affected by the bulk power used along with the ductility. Fractography images were also discussed and areas of interest with porosity and or surface notches were pointed out to give an overview of surface roughness in relation to fatigue testing.

4 Microstructural analysis of representative coupons for tensile bars and fatigue bars.

The following experiment was conducted by preparing representative metallographic coupons for the SEM. They were imaged to determine the microstructure present in samples representative of fatigue bars and tensile bars for material characterization. This was done to determine what aspects of microstructural features and defects including porosity effect the mechanical properties.

4.1 Methods

The following experiment proceeds in two parts: first microstructure and porosity are compared for samples with different bulk laser power, then the samples built with the same bulk laser power, but different build geometries are compared. In this experiment samples were polished as per the methods described below and imaged both at low magnification and high magnification with a Jeol JSM-7900F scanning electron microscope in electron back scatter to reveal the grain structure of the material and then compared qualitatively. The samples are also compared using EDS Niobium mapping and through a limited study of porosity using a Leica DMV 6 microscope.

4.1.1 Specimen Geometry

The following figure gives the Schematic of the representative metallographic coupons.

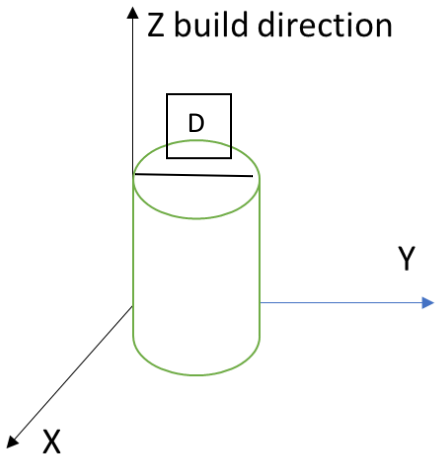

Figure 13: representative schematic for metallographic specimens with build direction defined and diameter D of 4mm or 5mm.

4.1.2 Additive Manufacturing Build parameters

The following table gives the build parameters that are of interest in this study along with the diameter of the samples for each build geometry.

Table 5: bulk laser power and build diameter for specimens tested in this study

specimen #	bulk power (W)	diameter (mm)
1	230	4.06
3	280	4.06
4	330	4.06
6	230	5
7	280	5
8	330	5

The build direction for all metallographic samples is defined in XYZ in the following figure.

4.1.3 Sample preparation

4.1.3.1 Cutting the metallographic samples

The samples were cut using an IsoCut Wafering Blade with a thickness of 0.015in and a blade diameter of 5in. The blade is first inserted into the saw. The saw blade is conditioned using the ceramic block provided within the packaging for the blade. This is done by placing the ceramic block into the sample clamp and then programing the saw to cut a length of 0.25 in into the ceramic block. The saw is programed by setting the blade speed to 300rpm, the auto cut speed to 0.05in/min, and the cutting distance to 0.25in. The hood is closed and the cutting cycle is started.

Once the blade is conditioned the ceramic block is removed from the specimen clamp and the specimens can be inserted into the clamp and so that the XY plane is

parallel to the saw blade. The thickness of the specimen must first be approximated to determine the cutting distance. A distance that is higher than the thickness of the specimen is recommended to ensure that it is cut all the way through. The saw blade and specimen clamp are aligned so that the specimen will be cut in half. The saw is then programed to cut through the specimen. This is done by increasing the blade speed to 3500rpm, leaving the auto cut speed at 0.05in/minute, and setting the cutting distance to close to 0.2in for the 4 mm diameter samples and close to 0.25in for the 5 mm diameter samples.

The samples were then removed from the mount and one half was glued using Gorilla super glue gel to a plastic fabricated mount so that the YZ plane of the sample is now parallel with the saw blade. The sample is pressed into the mount for 30s to 1min until the super glue dries and then left for 24 hours for the glue to fully cure. Once the glue has fully cured the mount is placed inside the specimen clamp so that the YZ plane of the sample is parallel to the saw blade. The saw is programed for with the cutting cycle. This is done by leaving the blade speed at 3500rpm, the auto cutting speed at 0.05in/min, and changing the cutting distance to 0.5 to 0.65in depending on the length of the remaining specimen.

Finally, once the specimen has been cut it is submerged in 100% acetone in a small beaker and left to sit in a vibratory bath until the specimen can be removed from the mount. Once the specimen is removed it is mounted using the Buehler Simplimet XPS1 mounting machine and the Epomet molding compound.

4.1.3.2 Polishing the specimens

The specimens were polished using a Buehler EcoMet 250 and Buehler polishing pads and solutions. First a Carbimet 240 SiC abrasive pad is placed on the wheel. Next, a specimen holder is locked into place in the head of the Auto-polisher and the head is positioned above the wheel and locked into place using the lever behind the head. The samples are placed face down in the sample holder. The time necessary for the first round of polishing is not specific and depends on how level the surface of the specimen is. The base speed was set to 300 rpm and the relative direction of the head is set such that the head and the wheel are moving in the same rotational direction. The force is set to 6 lbs and the cycle started.

The next steps in the polishing process are the same as the ones described above however different pads and polishing solutions are used. The next pad used is a Carbimet 320 SiC and the base speed is set to 300rpm, the force is set to 6lbs and the rotational direction of the wheel and the head is the same. The time is set to 3 minutes. An Ultrapad is then used, and the base speed is set to 150rpm, the force is set to 6lbs and the relative rotational direction of the head is changed so that it is the opposite of the base. The time is set to 5 minutes. A 9μm MetaDi Supreme Diamond slurry solution is used and sprayed periodically by hand on to the Ultrapad. The next pad used for the next three steps is the Trident pad. Each polishing solution is used with its own Trident pad. The time is set to 3 minutes, the force is set to 6lbs, and the relative rotational direction of the head is opposite to the base for all three steps. First the 6μm MetaDi Supreme Diamond is used, then the 3μm MetaDi Supreme Diamond is used, lastly the 1μm MetaDi Supreme Diamond is used. The final polish is done using a Chemomet pad and two different

polishing solutions. Both polishing steps have the time set to 2 minutes, the force set to 6lbs, and the relative direction of the head is opposite to the base. First the Mastermet 0.06μm colloidal silica is used, then finally the Mastermet 2 0.02μm colloidal silica.

During the polishing process sample 3 was lost due to over polishing. Sample three was fabricated with 280W and a 4.06mm diameter. As a result, all following comparisons between diameters are made only between 230W sample and 330W samples.

4.1.4 Microstructural Analysis

For both the SEM imaging and the EDS mapping the samples were first prepped by polishing until nearly all scratches were gone. As mentioned before Sample 3 was lost during polishing so comparisons based on build geometry going forward are made between 230W samples and 330W samples only. Each sample was then prepped for the SEM by cleaning off the surface with ethanol and a cotton swab and then using Soft Nitrile gloves the samples where mounted in a holder specific to the SEM. The chamber was vented, then opened, and the sample inserted. Air is evacuated from the chamber before the sample is put into the main chamber.

After this the program PC_SEM is opened. The Specimen is then inserted into the main chamber using the bar attached to the SEM. Once the sample is inserted the program will not allow for the electron bean to be turned on until the bar and handle are in a horizontal position again. Once the specimen is inserted the button in the program labeled Cam is used to bring up the internal camera. The Electron back scatter detector is inserted, and the specimen must be moved within range (10mm of the detector). While the sample is being moved into the proper range a hand must hover over the black track

ball in case it is necessary for an emergency stop. Once the sample is within range of the detector the electron beam can be switched on to start observing the sample.

4.1.4.1 SEM Imaging

Once the sample is in the SEM and able to be viewed by the SEM the settings for the probe current and Acceleration voltage must be changed to the following: Acceleration current (15.0kV), and probe current (11). This will give an emission current of 41.8μA. These settings were found to produce the best images in Electron back Scatter.

Using the fine 1 setting the image is focused. Focusing depends on the distance of the sample from the detector and the beam alignment and the steps necessary to achieve a good, focused image can vary but in general the SEM can be focused by turning the knob labeled focus until the image is focused at increasing magnifications. To achieve good focus its good practice to make sure that the live image can be focus at a magnification higher than the intended magnification. If necessary, the image can also be focused using the small knobs labeled x and y. These knobs change the beam alignment and may produce a more focused image if the image cannot be sufficiently focused using the large focusing knob.

Once the image is focused and the magnification set to 250X the viewing mode is changed to Back Scatter Mode or BED-C. The contrast and brightness will need to be modified to view the back scatter image. This is done using auto contrast and brightness, or ACB. This will automatically adjust the contrast and brightness so that the image in back scatter can be seen. In order to produce images with good contrast that reveals the grain structure the contrast and brightness can be adjusted manually by using the small knobs labeled contrast and brightness until the desired level of contrast is achieved.

Each sample was imaged near the center of the sample at 250x and at 5000x multiple times to get images that are representative of the microstructure present. The samples were also imaged several times at 250X and 5000X near the edges of the sample to observe the change in microstructure near the contour region.

4.1.4.2 EDS Mapping

Once the sample is in the SEM and a representative section of microstructure is selected at 5000x and focused as per section 4.1.4.1 the Team: texture and elemental Analytical Microscopy program can be opened. In order to use this program a login in must be created. When logging in EDS must be selected. Once the program is opened, mapping was selected. Once collect map is clicked the program will open a pop-up window that will allow for the elements of interest to be selected. For this study Nb, Mo and Ni were selected to show precipitate laves phases.

Once the elements have been selected the program will automatically start the scan. These scans were run at a resolution of 1024 X800 and a standard quality. These tests were also not left to complete the scan. This was done to ensure clarity of the laves phases as longer scans produced small shifts in the image that caused the previously clear laves phase segregation to blur. While the number of scans was different per sample in general around 30 scans was sufficient to produce quality images. The data was then exported the high-resolution image was saved.

4.1.5 Porosity Analysis

Each sample was prepared for imaging with the Leica DVM6 by polishing the surfaces as described above and cleaning the surface after polishing. Cleaning was done using 100% acetone in a fume hood with a cotton swab. The cotton swab was dipped into

the acetone solution and gently swabbed over the surface of the sample then another dry swab was used to dry up any remaining acetone.

4.1.5.1 Sample imaging

Once the samples were properly cleaned, they were imaged. This was done by first turning on the Leica DMV6. The sample was placed on the stage and the program Lecia LAS X was opened. The lighting was adjusted and set to use the full ring light. Next after ensuring that the live image button in the bottom left-hand menu is clicked the image is focused using the attached motorized dial and the brightness is adjusted using the slider bar in the Illumination tab [34]. The Magnification used for these porosity images was 200x. Once the live image is focused and sufficiently illuminated, images of representative porosity were taken in both the XY plane and the ZY plane. This was done by opening the file system within the program which brings up a pop-up window, creating an new file for each sample, selecting that file using the record file button in the menu at the top, naming each image in the text box at the very bottom, and finally clicking the capture image button at the bottom of the main window near the live image button [34].

4.1.5.2 ImageJ Porosity Analysis

Once the images have been saved, they can be analyzed in ImageJ. This was done by opening the ImageJ program then clicking on open under the file tab to open the desired image. The measurement tool in the program must be calibrated. This is done by using the line tool in the menu and drawing over the scale bar in the bottom right-hand corner of the image. Next, the measurements are calibrated by going to the analyze tab and then clicking on set scale command [35]. For these images the scale bar gives a

known distance of 500μm. The smallest units the program can set is mm so in the known distance text box a value of 0.5 was used and the units were set to mm. The same scale is used for each image analyzed in this study.

The image must be cropped before the analysis can begin. This is done by using the rectangular tool [35]. This will create a new cropped image that will automatically pop up. Next, the image was touched up to remove scratches which will otherwise interfere with data collection. This is done with the dropper tool and then the paint brush tool to cover up any scratches within the image [35]. The image must then be converted to grey scale [35].

Once the image is touched up and in grey scale it can then be prepared for analysis. This is done using the threshold tool. This will bring up a popup window that will turn the pores red in your image. The image was adjusted using the scale bar to ensure that all of the pores in their entirety are red [35]. This turns the image into a binary black and white image where the pores are white, and the sample is black.

To analyze the image the parameters were set to centroid area and ellipse. Next using the analyze tab the image can be analyzed and data can be collected. ImageJ will now automatically collect the necessary data [35]. Once the data pops up, a summary of the data was generated consisting of average pore size, minimum pore size, and maximum pore size. These values can then be used to compare the pore sizes within each sample.

4.2 Results

The following sections give the results of the experiment described above. This section does not include all of the microstructural images taken for this study.

4.2.1 Comparing samples based on bulk laser power used

Three bulk laser powers were used in this experiment 230W, 280W, and 330W. For the purpose of comparison only SEM images and EDS images from 230W and 330W will be used.

4.2.1.1 SEM BED-C microstructural results

The following figures show the results of SEM imaging in BED-C. All of the following images are from the bulk of the sample and are images of representative microstructure. Figure 14 shows the SEM images taken for samples with a diameter of 4mm built with bulk laser powers of 230W and 330W. Figure 15 shows the SEM images taken for samples with a diameter of 5mm built with bulk laser powers of 230W and 330W.

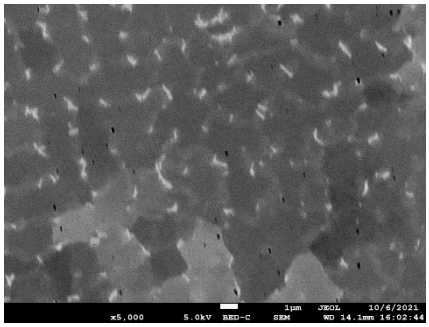

4mm 330W XY plane

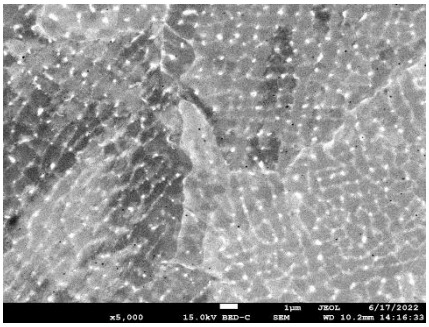

230 W 4mm XY plane

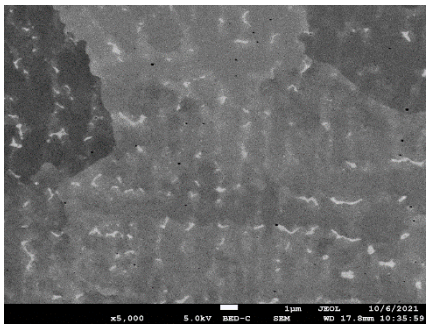

4mm 330W YZ plane

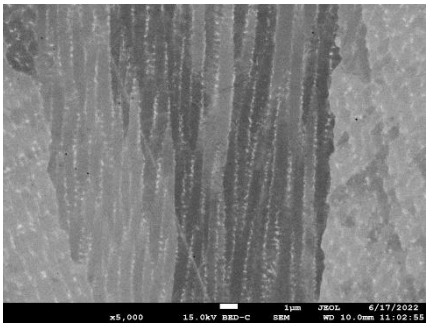

230 W 4mm YZ plane

Figure 14: BED-C images of samples built with 4mm diameter comparing samples made with 230W and 330W

The above image depicts the difference in microstructure seen between the samples fabricated with 330W and 230W with diameters of 4mm. Here the microstructure for parts fabricated with 330W is coarser than the microstructure seen in the 230W sample. In the 330W sample more energy is used which contributes to the cooling rate. Here the cooling rate is dependent on the amount of energy being input, the thermal conductivity of the material, the amount of material and the environment it is in. All images were taken from the bulk of the material so the environment for each location is similar the thermal conductivity of Alloy 718 is the same for all samples along with the size of the samples, or the amount of material present. So, the only change between these

samples is the amount of energy inputted. The samples built with higher laser powers input more energy into the system which causes a decrease in cooling rate. A decrease in cooling rate allows more time for the grains to grow, therefore creating specimens with coarser grains. The same phenomenon is seen in the figure below which compares samples fabricated with a 5mm diameter and bulk laser powers of 230W and 330W.

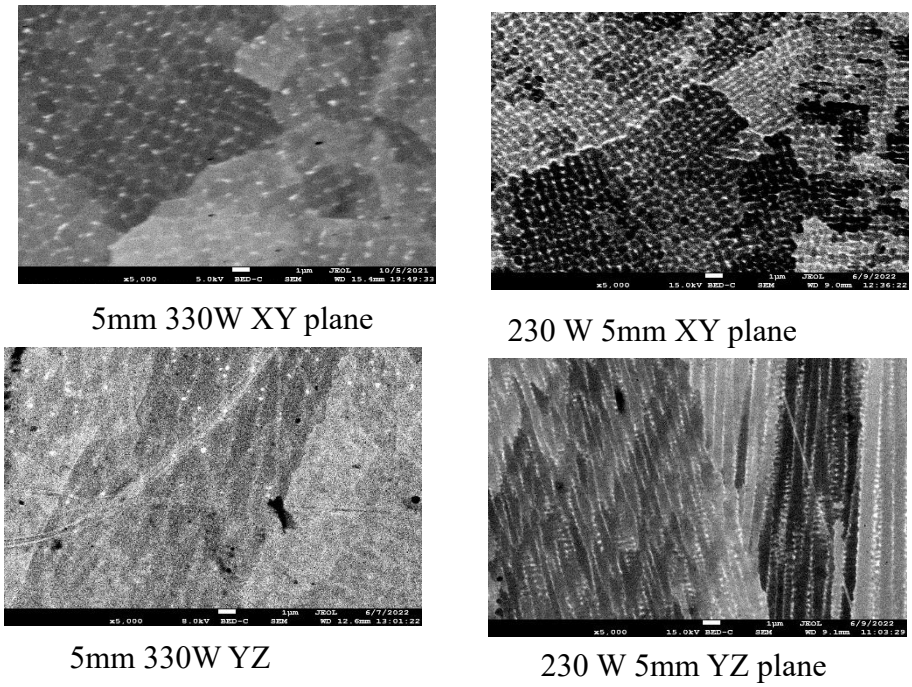

Figure 15: BED-C Images of samples fabricated with a 5mm diameter comparing samples made with 230W bulk laser power and 330W bulk laser power.

4.2.1.2 EDS results

The following images give the EDS Niobium maps for the metallographic samples. These were done using the SEM and used to visualize the segregation of Niobium within the 718 samples.

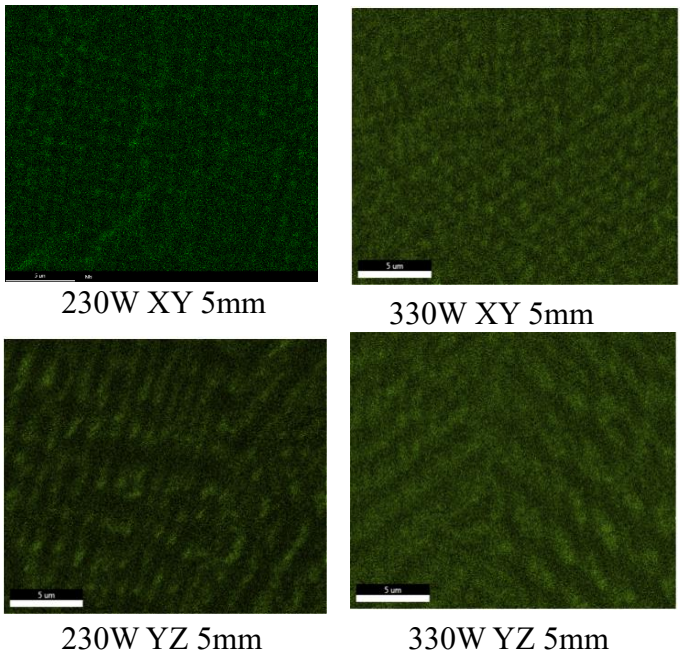

Figure 16:EDS Niobium mapping for samples made with 5mm diameter and bulk laser powers of 230W and 330W.

The above images give the niobium maps for samples made with a diameter of 5mm but different bulk laser powers. The powers used here were 230W and 330W. These maps show that the Niobium tends to be dispersed more finely in samples with 230W than for samples with 330W. This is due to the fact that Niobium tends to diffuse easily and laves phases tend to be thermodynamically stable during the solidification process.

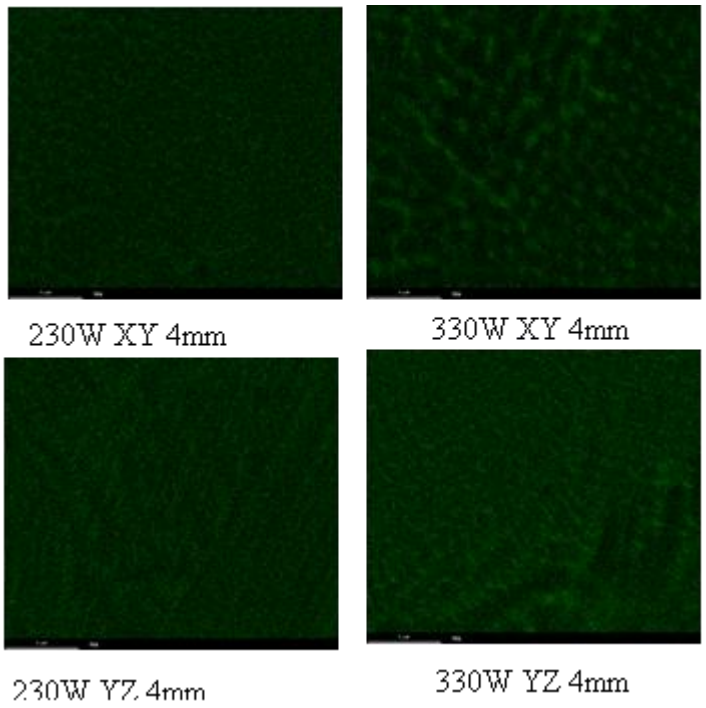

Figure 17: EDS images for 4mm diameter samples fabricated with 230W and 330.

The figure shown above is similar to the figure seen previously, however, these samples were built with a diameter of 4mm. Here the same observations as mentioned previously can be seen. Here the difference in Niobium segregation is more prominent in the XY plane for 4mm samples.

4.2.2 Comparing samples based on build geometry

The following results compare the representative microstructure of samples built with the same processing parameters but different build geometries. This is of particular importance to study for AM parts since AM can be advantageous for building parts with complex geometries. Due to different thermal histories seen by parts with different build geometries the material itself may not be the same. As a result, the mechanical properties for thin walled parts and thick walled parts may not be comparable.

4.2.2.1 SEM BED-C microstructural results

The following images compare the microstructures seen when comparing samples made with the same processing parameters but different build geometries. These images were taken from samples built with 230 W or 330 W and diameters of 4 mm and 5 mm.

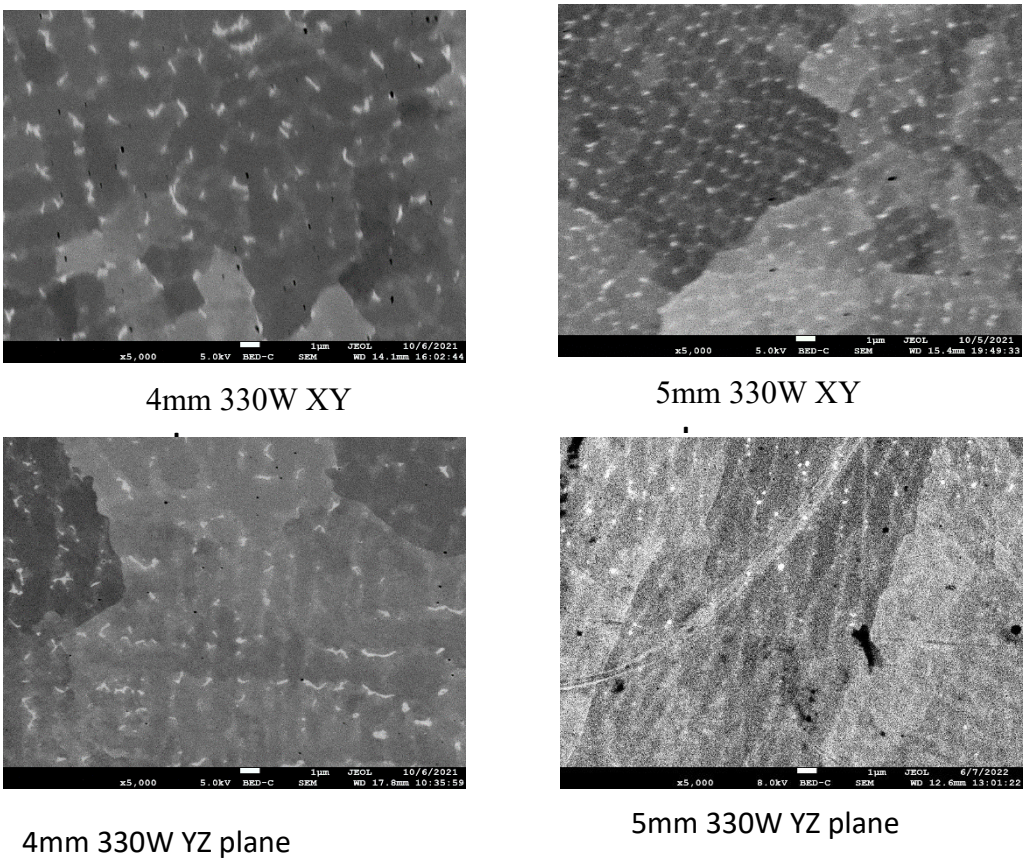

Figure 18: BED-C SEM images of XY and YZ for samples made at 330W with a diameter of 4mm and a diameter of 5mm.

The figure above shows the representative microstructure for samples made with 330 W and diameters of 4 mm and 5 mm. Here the sample made with 4 mm has coarser grains than the sample made with 5 mm. This is due to a difference in cooling rate. Here the amount of energy inputted into the system is the same for both samples, because the

bulk laser power used is the same. The thermal conductivity of Alloy 718 has not changed. The only element that has changed is the amount of material. Because of this the cooling rate for smaller samples is lower than the cooling rate for larger samples thus allowing grains in smaller samples time to grow.

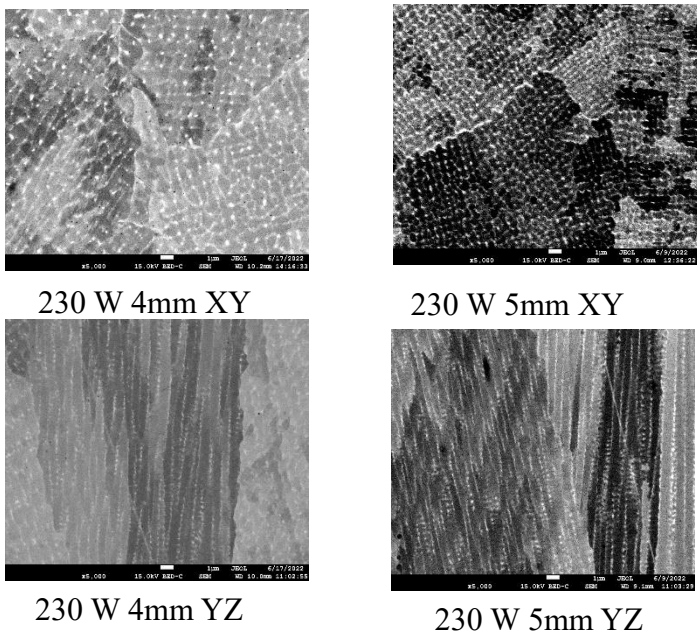

Figure 19: BED-C SEM images for samples fabricated with 230W and diameters of 4mm and 5mm.

4.2.2.2 EDS results

The following figures show the results from EDS Niobium mapping for samples fabricated with different build geometries but the same build parameters. The following figure shows the results from the EDS scans for samples fabricated with 330W.

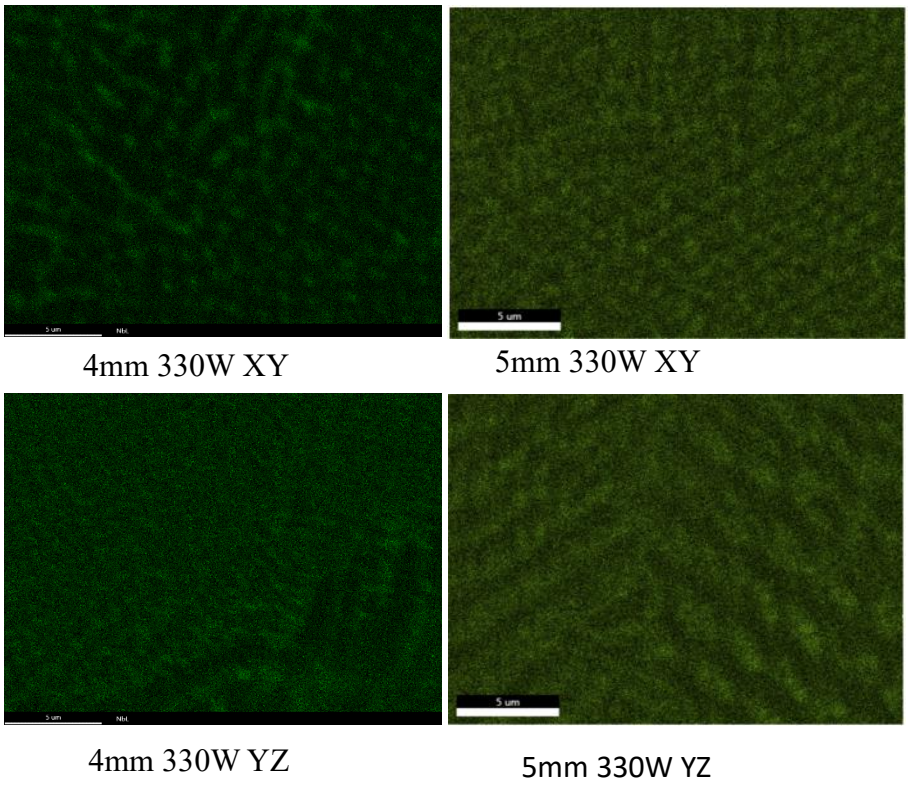

Figure 20: EDS maps of Niobium distribution for samples fabricated with 330W and diameters of 4mm and 5mm

Here in the XY plane the difference in Niobium segregation is very clear. The smaller sample has more niobium segregation than the larger sample, however in the YZ plane the difference is not as clear. Both mapping images clearly have areas where the texture seen for the Niobium segregation changes indicating non-uniform diffusion in the smaller samples.

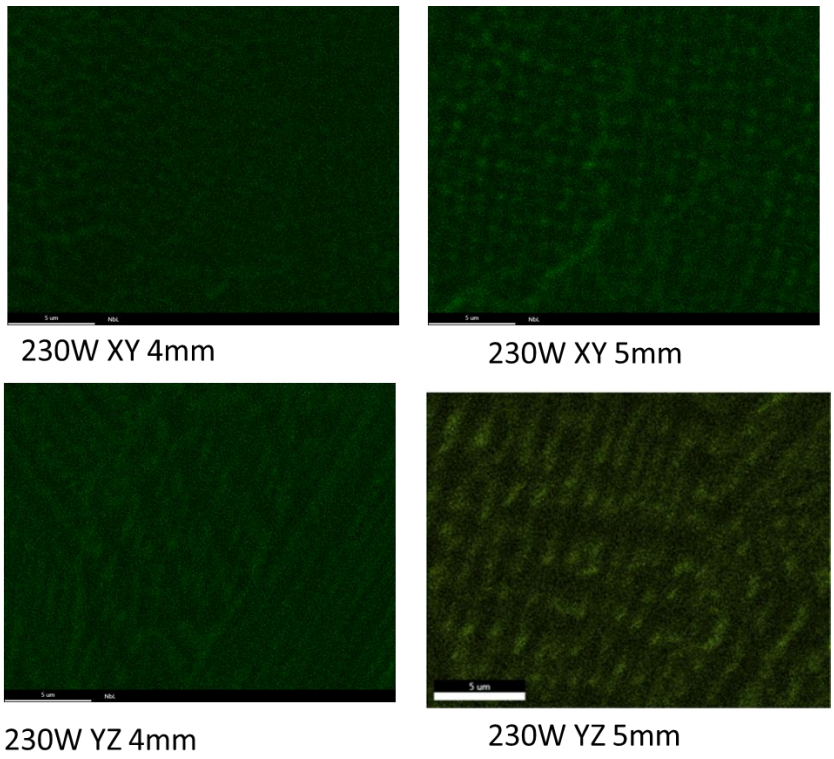

Figure 21: EDS niobium maps of samples made with 4mm and 5mm diameters fabricated with 230W bulk laser power.

The figure above shows the Niobium maps for samples fabricated with 230W and diameters of 4mm and 5mm. Here the Niobium segregation between the two samples is very similar, especially in the XY plane. However, there are differences to be seen between the samples in the YZ plane. Here the Niobium is more finely dispersed.

4.2.2.3 Porosity results

The following images show the representative porosity for samples built with 230W and 330W, and 4mm and 5mm diameters.

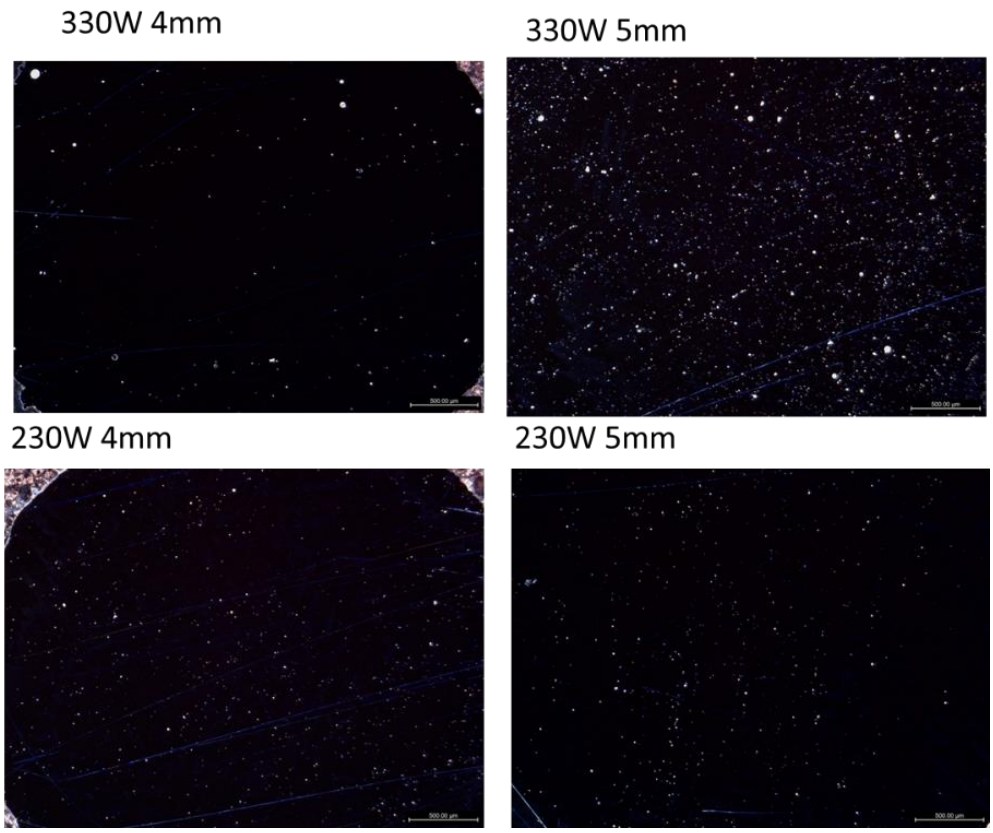

Figure 22: Images of representative porosity seen in samples fabricated with diameters of 4mm and 5mm built with 230W and 330W bulk laser power.

Upon visual inspection the samples built with 330W appear to have more pores than samples built with 230W. While the porosity percentage is important the size of the pores can give an idea of how porous the samples are the size of the pores have a huge impact on the mechanical properties [26]. This is important for both the fatigue life and the tensile properties and can provide some insight into how the defects along with the microstructure effects the mechanical properties.

The following table shows the relevant data for pore size including the average pore size, the minimum pore size, and the maximum pore size.

Table 6: Table of Porosity data: Build parameters and samples size, mean pore size, minimum pore size, and maximum pores size.

bulk laser power (W)	diameter (mm)	mean pore size (µm)	minimum pore size (µm)	maximum pore size (µm)
230	4	21.03	7.75	66.69638403
330	4	41.12	7.75	228.1467848
230	5	26.1158614	7.75	213.0159529
280	5	25.42880657	7.75	216.8095234
330	5	27.42447649	7.72	215.690271

This table shows that the sample with the highest mean pore size was built using 330W and a diameter of 4mm. This sample also has the highest maximum pore size. The 4mm diameter samples represent the gauge section of the fatigue bars. This aligns with the fatigue data seen previously in section 3.1.4. The higher porosity seen in higher power samples is most likely due to keyholing effects normally caused by increased laser power.

4.3 Conclusions

This section showed using SEM BED-C images that the coarseness of grains increases with both increasing laser power and smaller sample sizes. Here more laves phase segregation was also seen in samples built with higher laser powers and smaller sample sizes as seen in the EDS maps. The porosity study revealed that the samples with the highest porosity tends to be samples built with higher powers specifically for the fatigue diameter samples.

5 Microhardness testing

While microhardness testing is generally used to give insight into the hardness on the surface of a material it can also be used to give insight into other material properties as well [16]. Microhardness data can also be used to determine strength and other mechanical properties as well as give insight into grain size [16] and [36]. In general, microhardness values tend to increase for finer, smaller grains and decrease for coarser, larger grains [36]. Microhardness can be tested using two different micro-indenters namely the Knoop indenter and the Vicker's indenter [37]. The indenter used in this work is the Vicker's indenter. This indenter creates square symmetrical indents and the hardness values from this test are usually reported in HV [38]. The standard for this indenter is to space the indents a minimum of 2.5 times the length of the diagonal of the indent [37]. The indents were spaced by 150μm in this study due to the volume of indents required for the area arrays.

5.1 Overview of experiment

This test was conducted using a Buehler microhardness tester, Wilson Diamet VH1202 using a Vicker's tip with an HV 0.05 value, and the associated Diamet Software. Each sample was cut along the XY plane and the YZ plane, using Buehler's Isomet 5000 Linear Precision saw and polished using Buehler automatic polishing, EcoMet 250 Grinder Polisher, equipment. Each plane of the samples was then tested using the Buelher microhardness tester. Each specimen was tested using a line test with the indents 150μm

apart from edge to edge across the sample. These line tests were repeated 3 times per sample. Each sample also was tested using a matrix array of indents that did not cover the entire sample. Each array spanned from edge to edge in the y direction and each array was done in a similar section of each sample with respect to the center of the sample.

The number of indents varied based on the geometry of the sample and the plane in which the microhardness values were taken. This was done to minimize the number of indents created on the mount medium. All indents made on the mount medium or touching the edge of the sample where it interfaced with the mount medium were excluded from the results as they are not representative of the hardness of the sample itself. Some indents experienced a computer error when the automated measurement algorithm measured the indent. These were corrected manually in order to reflect the correct hardness value. An Example of this is given in the following figure.

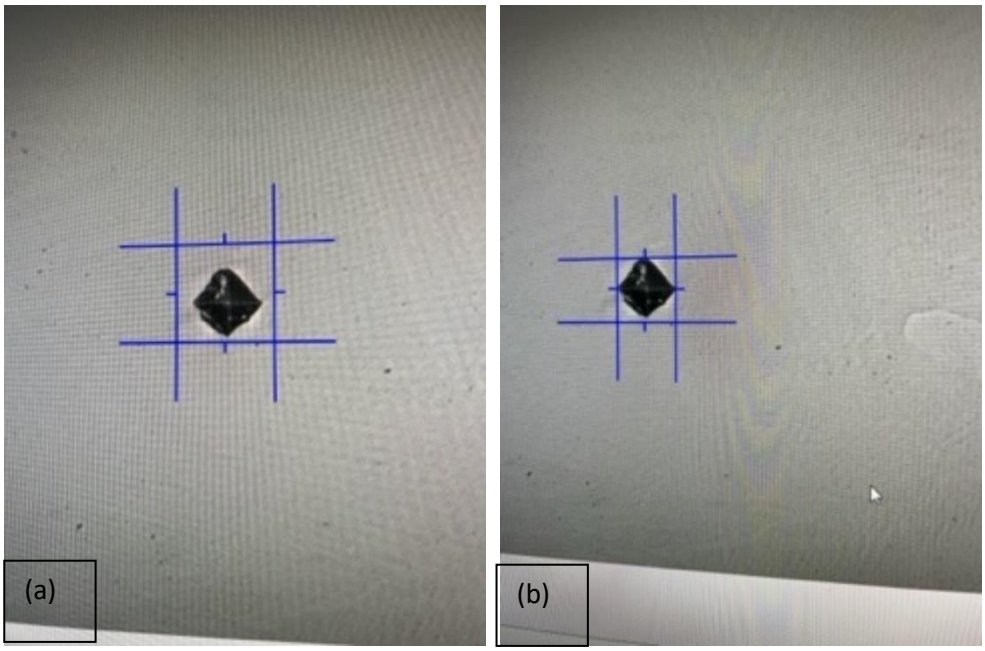

Figure 23:Figure showing an example of the computer error seen when measuring indents (a) shows the computer-generated measurement for the size of the indent, (b) shows the manually corrected measurement

Each test was then exported as an excel file and imported into MATLAB so that the data could be graphed in 2D or 3D scatter plots. These plots were used to compare the hardness values across different samples which were built with different build geometries and different bulk laser powers. Averages for the microhardness values for both the line tests and the area arrays were also calculated for comparison.

5.2 Build parameters

The specimens used in the above experiment were built using the Open Additive Panda machine. All specimens were built with the same contour laser power, contour laser speed, and bulk laser speed but the bulk laser power and geometry were changed. In this experiment the following parameters were used to fabricate the specimens using laser powder bed fusion.

Table 7: table representing the metallographic specimens and their build parameters

Specimen No	Contour Power (W)	Contour Speed (mm/s)	Bulk Power (W)	Bulk Speed (mm/s)
METALLOGRAPHIC COUPONS				
1	150	560	230	800
2	150	560	230	800
3	150	560	280	800
4	150	560	330	800
5	150	560	230	800
6	150	560	230	800
7	150	560	280	800
8	150	560	330	800

Here the build direction is defined as the Z direction and is the same as the build orientation mentioned in section 4.1.1.

5.3 Methods

The experiment described above was conducted using the following basic steps: first the samples were cut the XY plane and the YZ using the Buehler Isomet 5000 Linear Precision Saw as seen in section 4.1.3.1, second the samples were polished using the Buehler Automatic EcoMet 250/30 Grinder Polisher as seen in section 4.1.3.2, and finally

the samples tested using the Wilson VH1202 microhardness tester and the associated Diamet software.

5.3.1 Microhardness testing to compare representative metallographic coupons for fatigue bars and tensile bars

Fist the microhardness tester is turned on, the computer is booted up, and the program labeled Diamet is opened. Login to the Diamet platform by ensuring that the drop-down menu has admin selected. After this the Buehler Ez-clamp is used. This ensures that the specimen is level during the test. The sample is inserted into the Ez-clamp and then the clamp is secured onto the stage of the Microhardness tester.

When in the home page a new program can be created by typing the name of the program into the text box under programs and hitting the plus button [38]. Three different programs were made, line tests, area tests for the plane parallel to the build direction, and another for area tests for the plane perpendicular to the build direction. The line test programs are created by going to the section labeled “type” and clicking on location testing. The pattern is set to single row. The number of indents is specified in the text box labeled “indents (n1)“ [38] and the number of indents in this study varied for each build geometry but in general 27 indents were used for 4mm diameter samples and 34 where used for 5mm samples. The distance between indents was always kept the same at 150μm using the text box labeled indent space (b1) [38]. These tests were conducted using vicker’s hardness. Finally, the section labeled pdf is opened. Excel files must also be enabled and the test boxes in these sections must be filled out for each test in order for the files to be exported with the proper names.

Each area array is created the same way. A new program is made for each plane and labeled accordingly, the program is changed to location mode and matrix is selected in the drop-down menu for the pattern. Rows (n1) allows for the user to input the number of rows, Columns (n2) allows for the user to input the number of columns [38]. For these tests the number of rows depends on the build geometry and the number of columns depends on the plane being tested. The number of rows for the 4mm samples is 27, the number of rows for the 5mm is 34, the number of columns for the plane perpendicular to the build direction 10, and the number of columns for the plane parallel to the build direction is 20. These tests were also run with Vicker's hardness indenter.

All three tests were conducted on the samples and were done using a value of 0.05HV. Three-line tests were run on each plane for a total of 6 per sample and they were run from edge to edge in the y direction on the left side of the samples. The Area tests were run once on each plane so a total of twice per sample. These were done by placing the first indent near the edge and the rest of the indents proceeding in a matrix array down and towards the right of the sample. Finally, in order to normalize the data exported so that the coordinates are in relation to the sample. This was done by recording the coordinate data for the edge closest to the first indent for each line test and the edges on all four sides for the area tests. The line tests were normalized in respect to their distance to that edge point. The area tests were normalized by calculating the center point based on the edge coordinate data and then normalizing the area data points based off of the center of the sample.

All the data was graphed using MATLAB as scatter plots the hardness values that were less than 100 were removed as the represented indents interacting with porosity or

the mount medium. The averages for each test were recalculated in their excel sheets after these extraneous points were removed. As mentioned in section 5.1 some of the indents were not measured properly by the machines automated system so these were corrected manually while the tester was running the experiment.

5.4 Results

The following figures show the results from the Microhardness testing, while line tests were also conducted those results are given in Appendix. The following figure compares the Microhardness area arrays taken in the XY plane for samples made with 230W, 280W, and 330W.

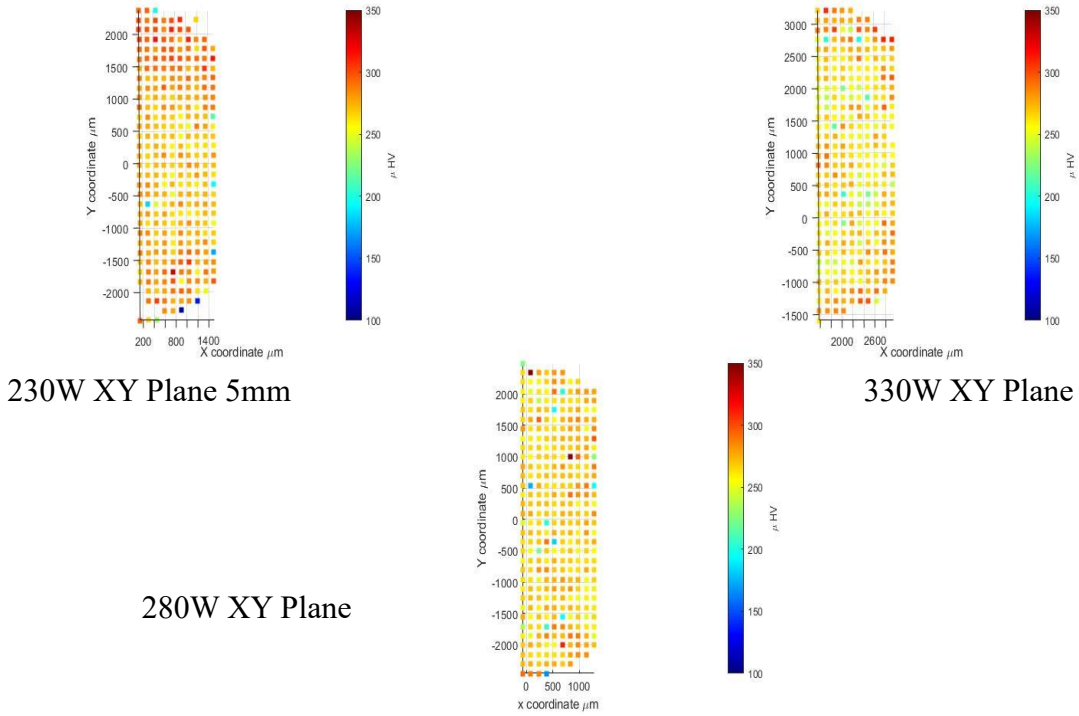

Figure 24: Microhardness maps for 5mm samples with bulk laser powers of 230W, 280W, and 330W. These are all in the XY plane.

Here it is clear that the hardness values vary a crossed the area tested within the XY plane for all samples shown here. This means that there is spatial variation in Microhardness within the sample. As discussed before these results also give insight into the microstructure seen within these samples. Larger grains result in lower hardness values than smaller grains, thus spatial variation in Microhardness values also indicated a spatial variation or inhomogeneity in grain size throughout the sample. These arrays also show that in general the microhardness is lower for samples built with higher powers because of coarser grains further proving results seen in section 4.2.1.1.

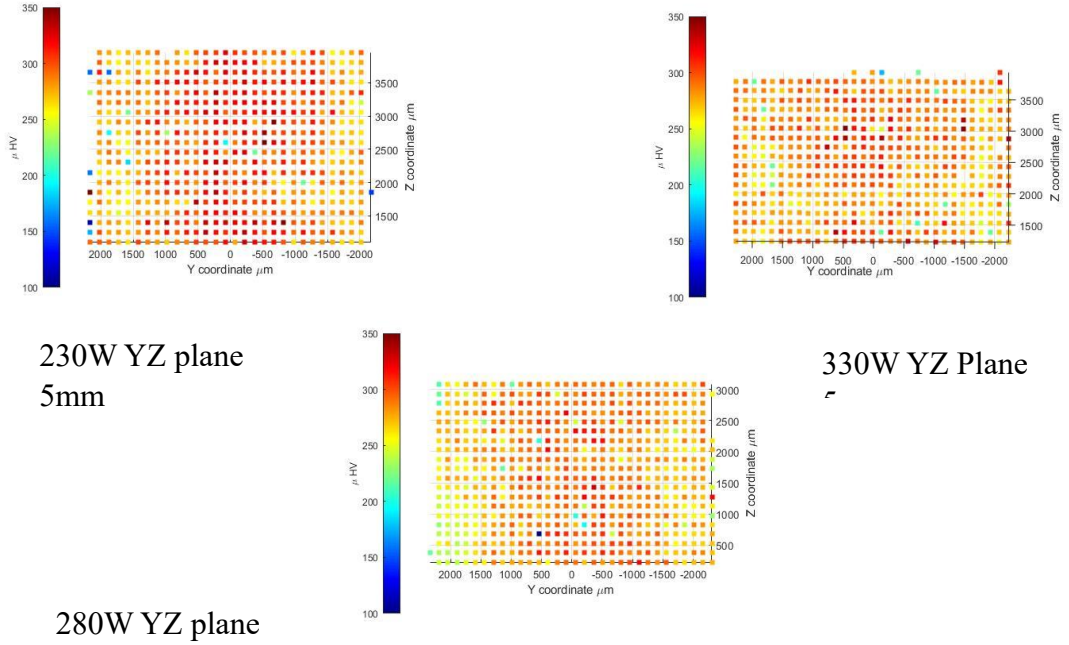

Figure 25: microhardness maps for samples made with 5mm diameters and bulk laser powers of 230W, 280W, and 330. These are all from the YZ plane.

The figure above shows the area arrays for the YZ plane for samples fabricated with 230W, 280W, and 330W. Again, here the microhardness varies spatially across the sample and the areas near the middle of the sample is harder than the area near the edges of the sample. This shows that the grains near the center of the sample are finer and is due to a difference in cooling rate due to the environment the material near the center encounters. Here, higher powers tend to have lower hardness values and based on visual inspection there is little difference in hardness between the 280W sample and the 330W. The difference in the microhardness between powers is not easy to visualize with the area arrays shown here so, later in this section a discussion of the average hardness values for all samples.

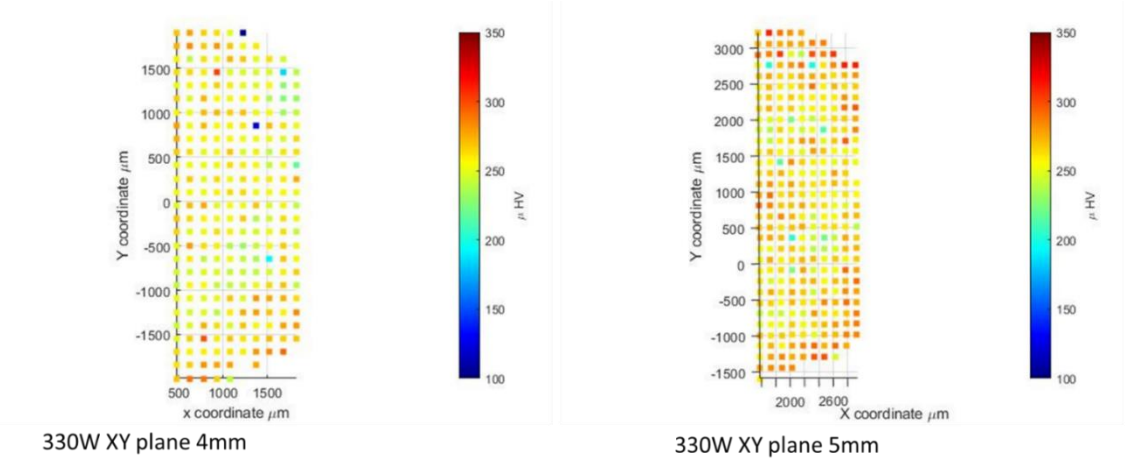

Figure 26: Microhardness maps for 4mm and 5mm diameter made with 330W bulk power. These were taken in the XY plane

The above figure compares the microhardness arrays for samples made with the same build parameters but different diameters in the XY plane. Here upon visual inspection the smaller sample has lower hardness values compared to the larger sample

which shows that it has larger grains despite being fabricated with the same processing parameters. This is due to a difference in cooling rate.

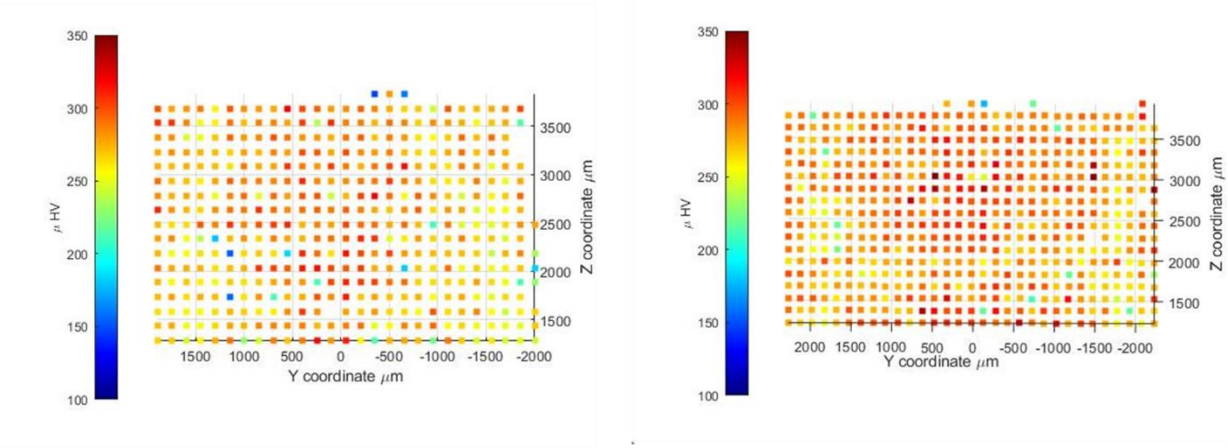

330W YZ plane 4mm

330W YZ plane 5mm

Figure 27:microhardness maps for 4mm and 5mm made with 330W. these were taken in the YZ plane.

The images above show the difference in hardness values for the area maps taken on samples built with 330W bulk laser power but different diameters in the YZ plane. Here the microhardness is again lower for the smaller sample due to larger grains than it is in the larger sample. Just like in

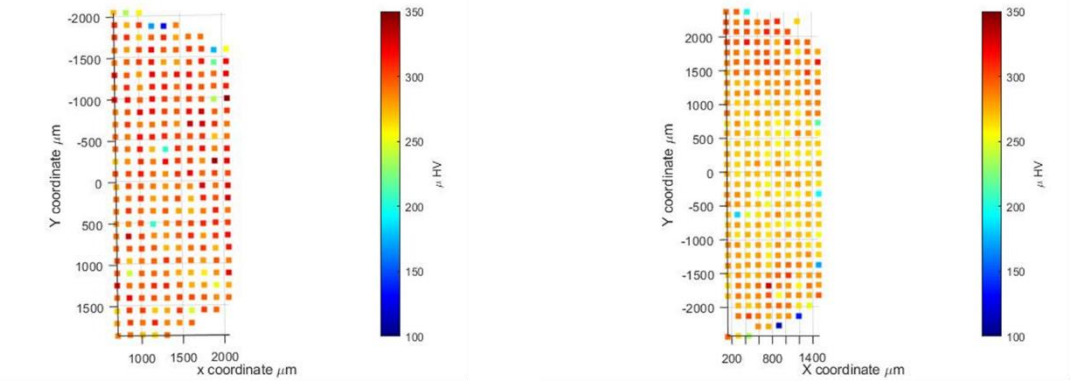

230W XY plane 4mm

230W XY plane 5mm

Figure 28 and Figure 29 the material is harder near the center of each sample due to the change in cooling rate.

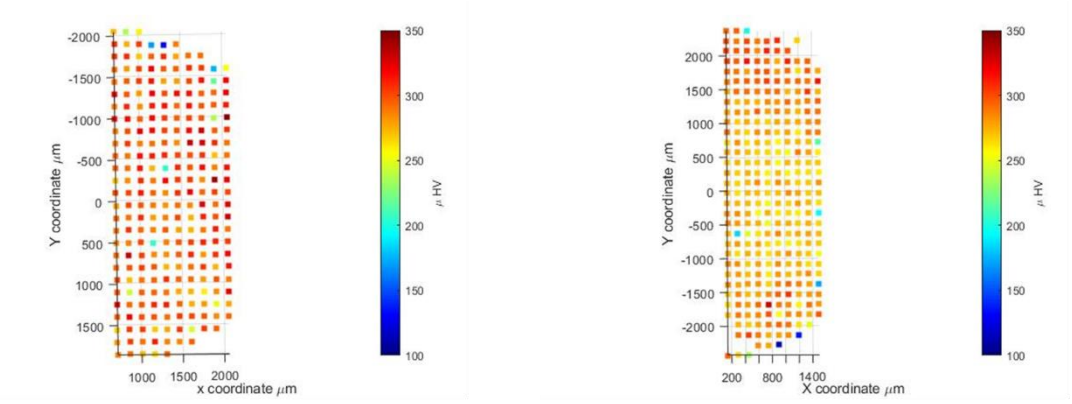

230W XY plane 4mm

230W XY plane 5mm

Figure 28: Microhardness maps of 4mm and 5mm diameter samples made with 230. These were done on the XY plane.

The area maps shown above were taken on the XY plane for samples made with 230W but different build geometries. Here the hardness vales for the smaller sample are higher than they are for the larger sample. This is the opposite trend to what was seen earlier for 330W samples and is not what is expected based on the SEM images discussed in section 4.2.2.1. This can be explained by an increase in error for the test run on the smaller sample in this plane. Here the standard deviation is 24.34.

In the images below the microhardness maps for the YZ plane for samples built with 230W and different build geometry the microhardness values are lower for the smaller sample in contrast to the data seen above. This aligns with the data seen

previously in the SEM images and with higher power samples. Therefore, the error in these data sets is pulled into question. The microhardness data in both planes of the smaller sample should be similar however the standard deviation mentioned previously is the higher when compared to the standard deviations of the other data sets.

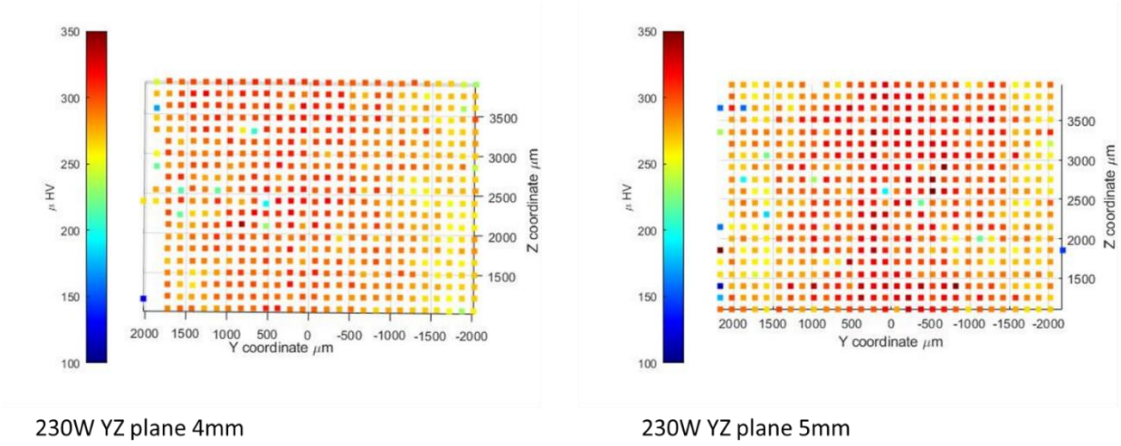

Figure 29: Microhardness maps for samples made with 4mm and 5mm diameters fabricated with230W. These were done on the YZ plane.

The following data gives a summary of the microhardness results including the averages for each sample.

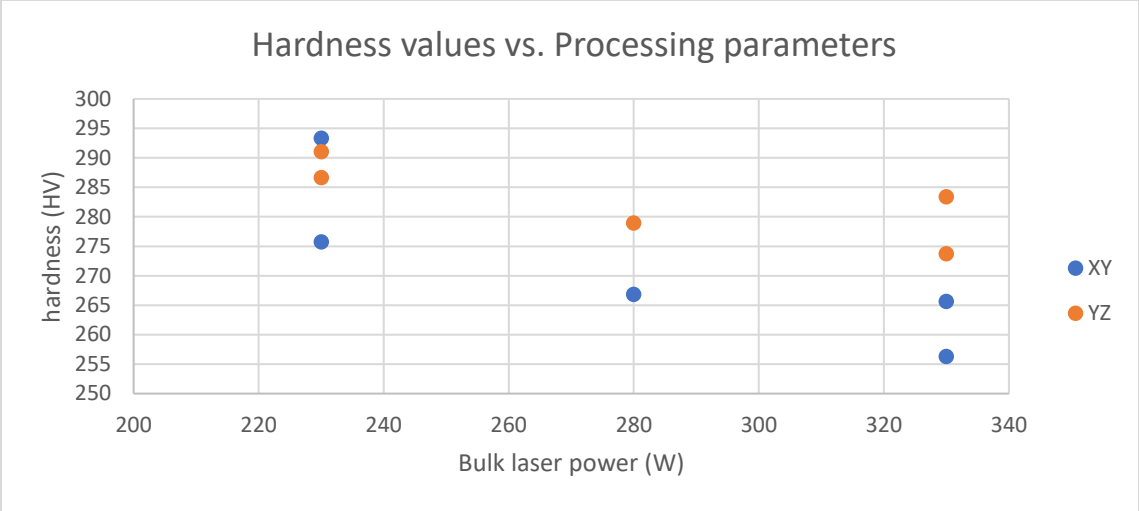

Figure 30: Graph showing the average hardness values for each sample based on power. The blue points are the average values from the XY plane, and the orange points are average values for the YZ plane.

The graph above shows the average hardness values for all samples. Here its much clearer that the hardness values for higher powers tends to be lower than samples made with lower powers due to differences in cooling rates. Here the hardness in the YZ plane also tends to be higher than the hardness seen in the XY plane. Below is the average hardness data based on both bulk power and sample size. Here it's clear that smaller samples tend to have lower hardness values due to coarser grains aside from the XY plane in the smaller sample made with 230W. The standard deviation for this data set however is higher than any of the others indicating that it is not entirely comparable.

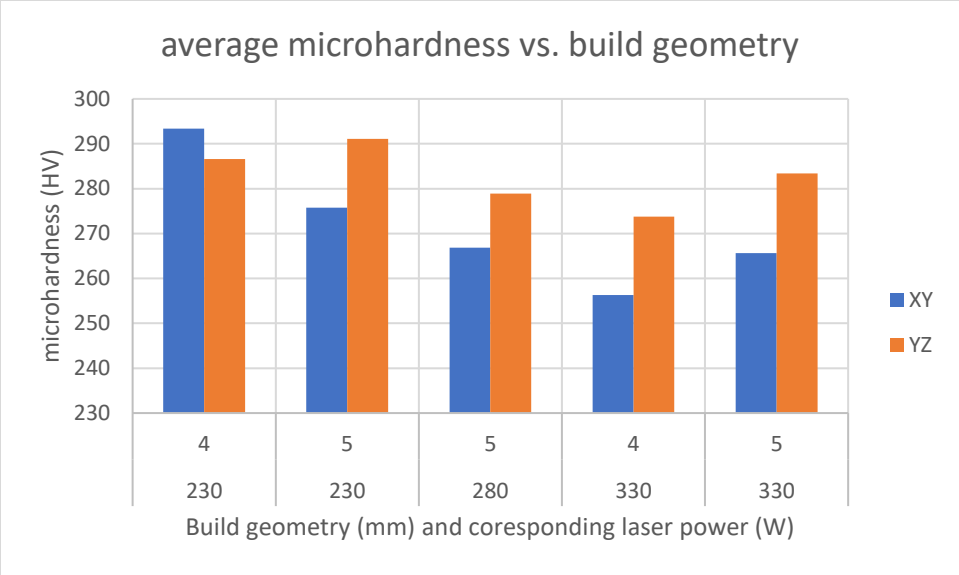

Figure 31: Average Microhardness for samples with 4mm and 5mm diameters built with 230W, 280W, and 330W bulk laser power.

5.5 Conclusions

In the sections above many conclusions can be drawn. First it is clear that all samples in both planes experience spatial variation in microhardness as a result of inhomogeneous microstructure. The average hardness values also decrease with increasing power and samples made with the same processing parameters with different build geometries experience different hardness values. Specifically, smaller samples tend to have lower hardness values than larger samples. The results of the hardness testing confirm some of the SEM images seen in other sections.

6 Conclusions and future work

This work focused on material characterization of Alloy 718 and representative coupons for the gauge sections for fatigue and tensile bars. Here, the cycles to failure have been found to decrease as the bulk laser power decreases. Surface roughness, porosity and microstructure all influence this outcome. The finer grains contribute to the strength of Alloy 718 however the bulk laser power appears to only effect the ultimate tensile strength. From these results it can be seen that the parts fabricated with higher bulk laser powers have lower ultimate tensile strengths. The ductility and yield strength of these samples does not depend on the processing parameters.

Form the materials characterization perspective the samples were not only shown to have coarser grains for samples built with higher powers, but smaller samples (fatigue diameter) were also found to have coarser grains than larger samples (tensile diameter). This data was supported with microhardness testing. The microhardness testing not only revealed that higher power samples and smaller samples have lower hardness values due to larger grains, but they also show considerable spatial variation in hardness indicating inhomogeneous microstructures. The results found in this work can be further studied and quantified using methods such as EBSD to determine grains sizes based on both bulk laser power and on specimen geometry.

While this study primarily focuses on materials characterization there are other aspects that can affect mechanical properties. Two aspects that are touched on in this

study but not investigated in depth are surface roughness and porosity. Surface roughness has a strong effect on fatigue life in particular so a quantifiable study on surface roughness in regards to fatigue life will contribute to future work along with more in-depth porosity studies.

This work showed three important things. Microhardness varies spatially throughout the samples indicating inhomogeneous microstructures in Alloy 718. Higher bulk laser powers result in samples with coarser grains and more Niobium segregation which impacts mechanical properties. Different sized samples built with the same processing parameters have different microstructures which suggests that the mechanical properties for tensile samples and fatigue samples may not be comparable.

References

[1] S. Pfeiffer, K. Florio, P. D, M. Grasso, M. Colosimo B., G. Aneziris C., K. Wegner and T. Graule, "Direct Laser Additive Manufactuing of High Performance Oxide Ceramics: a State of the Art Review," *Elsevier Ltd.,* 2021.

[2] D. Grossin, A. Monton, P. Navarrete-Segado, E. OzMen, G. Urruth, F. Maury, D. Maury, C. Frances, M. Tourbin, P. Lenormand and G. Bertrand, "A Review of Additive Manufacturing of Ceramics by Powder Bed Selective Laser Processing (sintering/melting): Calcium Phosphate, Silicon Carbide, Zirconia, Alumina, and their Composites," *Elsevier Ltd,* 2021.

[3] E. Hederick, "Additive Manufacturing of Metals: A Review," *Materials Science and technology,* vol. EWI, 2011.

[4] S. L. Sing, S. Huang, G. D. Goh, C. F. Tey and W. Y. Yeong, "Emerging Metallic Systems for Additive Manufacturing: In-situ Alloying and Multi-metal Processing in Laser Powder Bed Fusion," *Progress in Materials Science ,* vol. 119, no. 100795, 2021.

[5] M. J. O'Brien, "Development and Qualification of Additively Manufactured Parts for Space," *Optical Engineering, Department of Structural Mechanics,* vol. 1, no. 58, 2019.

[6] T. DebRoy, L. Wei H, S. Zuback J, T. Mukherjee, J. W. Elmer, J. O. Milewski, A. M. Beese, A. Wilson-Heid and W. Zhang, "Additive Manufacturing of Metallic Components-process, Structure and Properties," *Progress in Materials Science,* vol. 92, pp. 112-224, 2017.

[7] A. Porter D, E. Easterling and M. Y. Sherif, Phase Transformations in Metals and Alloys, Boca Raton, Fl: CRC Press Taylor and Francis group, 2009.

[8] E. Olakanmi, R. Cohrane and K. Dalgarno, "A Review on Selective Laser Sintering/melting of Aluminium Alloy powders: Processing, Microstructure, and Properties," *Progress in Materials Science,* vol. 74, pp. 401-477, 2015.

[9] H. K. D. H. Bhadeshia, M. Peet and S. Ooi, "Nickel Based Superalloys," University of Cambridge, Queen Mary University of London, 2003. [Online]. Available: www.phase-trans.msm.cam.ac.uk/2003/superalloys.html. [Accessed 19 June 2022].

[10] S. Hong, W. P. Chen and W. Wang T, "A Diffraction study of the Y'' Phase in INCONEL 718 Superalloy," *Metallugical and Materials Transactions A,* vol. 32A, 2001.

[11] E. Hosseini and V. A. Popovich, "A Review of Mechanical Properties of Additively Manufactured INCONEL 718," *Additive Manufacturing,* vol. 30, 2019.

[12] ASM Aerospace Specification Metals Inc., "Subcategory: Metal; Nickel Base; Superalloy," [Online]. Available: https://asm.matweb.com/search/specificmaterial.asp?bassnum+NIHC34. [Accessed 20 June 2022].

[13] O. Gokcekaya, T. Ishimoto, S. Hibino, J. Yasutomi, T. Narushima and T. Nakano, "Unique Crystalographic Texture Formation in INCONEL 718 by Laser Powderbed Fusion and its Effect on Mechanical Anisotropy," *Acta Materialia Inc.,* vol. 212, 2021.

[14] F. Brenne, A. Taube, M. N. S. Probstle, D. Schwarze, M. Schaper and T. Niendorf, "Microstructural Design of Ni-Based Alloys for High-temperature Applications: Impact of Heat Treatment on Microstructure and Mechanical Properties After Selective Laser Melting," *Prog. Addit. Manuf. ,* vol. 1, no. 3, pp. 141-151, 2016.

[15] Z. Wang, K. Guan, M. Gao, X. Li, X. Chen and X. Zeng, "The Microstructure and Mechanical Properties of Depositied- IN718 by Selective Laser Melting," *J. Alloys Compd. ,* vol. 513, pp. 518-523, 2012.

[16] C. Lesko, L. Sheridan and J. E. Gockel, "Microhardness as a Function of Process Parameters in Additively Manufactured Alloy 718," *Materials Engineering and Preformance,* vol. 30, no. 9, 2021.

[17] R. Konecna, L. Kunz, G. Nicoletto and A. Baca, "Long Fatigue Crack Growth in ICONEL 718 Produced by Selective Laser Melting," *International Journal of Fatigue,* vol. 92, pp. 499-506, 2016.

[18] S. Gribbin, J. Bicknell, L. Jorgensen, I. Tsukrov and M. Knezevic, "Low Cycle Fatigue Behavior of Direct Metal Laser Sintered INCONEL Alloy 718," I*nternational Journal of Fatigue,* vol. 93, pp. 156-167, 2016.

[19] S. S. Babu, N. Raghavan, J. Raplee, S. J. Foster, C. Frederick, M. Haines, R. Dinwiddie, M. K. Kirka, A. Plotkowski, Y. Lee and R. Dehoff, "Additive Manufacturing of Nickel Superalloys: Opportunities for Innovation and Challenges Related to Qualification," *Metal Material Transformations: A,* vol. 49, no. 9, pp. 3764-3780, 2018.

[20] V. V. Bolotin, Mechanics of Fatigue, Raton Florida: CRC Press, 1999.

[21] F. Beer, J. Dewolf, J. E. Jonhnston and D. F. Mazurek, Mechanics of Materials (8th ed.), New York: McGraw Hill, 2020.

[22] S. Shao and N. Shamsaei, "Synergistic Effects of Defects and Microstructure Fatigue Behavior of LB-PBF Metal Materials," in *TMS2020 149th Annual Meeting and Exhibition*, 2020.

[23] N. Hrabe, J. Benzing, R. Rentz, T. Gnaupei-Herold, Q. T, L. Koepke, J. Splett and F. DeiRio, "Fatigue Behavior of Additively Manufactured Titainium: Effects of Internal Porosity, Residual Stress, and Crystallographic Texture," in *TMS2020 149th Anual Meeting and Exhibition*, 2020.

[24] A. Balachandramurthi, J. Moverare, N. Dixit, D. Deng and R. Pederson, "Microstructural Influence of Fatigue Crack Propagation During High Cycle Fatigue Testing of Additively Manufactured Alloy 718," *Materials Characterization,149,* pp. 82-94, 2019.

[25] C. Kantzos, J. Pauza, R. Cunningham, S. P. Narra, J. Beuth and A. Rollett, "An Investigation of Process Parameter Modifications on Additively Manufactured Inconel 718 Parts," *Materials Engineering and Preformance,* vol. 28, no. 2, pp. 620-626, 2019.

[26] L. Sheridan, "Primary Processing Parameters and thier Influence on Porosity and Fatigue Life of Additively Manufactured Alloy 718," *Dissertation, Wright State University,* pp. 1-127, 2020.

[27] G. Dieter, Mechanical Metalurgy, New York Toronto London: McGraw-hill book company, 1961.

[28] P. Church, M. Reynolds, P. Gould, R. Oakley, N. Harrison, B. C. Williamson and N. Taylor, "Tensile Properties of AM Maraging Steel," *DYMAT 2018- 12th International Conference on the Mechanical and Physical Behavior of Materials Under Dynamic Loading,* vol. 183, p. 6, 2018.

[29] W. Everhart, E. Sawyer, T. Neidt, J. Dinardo and B. Brown, "The Effect of Surface Finish on Tensile Behavior of Additively Manufactured Tenisle Bars," J*ournal of Materials Science,* vol. 51, no. 8, pp. 3836-3845, 2016.

[30] A. Ni, C. Chen, X. Wang, P. Wang, R. Li, L. Zhang and K. Zhou, "Ansiotropic Tesnile Behavior of in situ Precipitaion Strengthened INCONEL 718 Fabricated by Additive Manufacturing," *Material Science Egneineering: A,* vol. 701, pp. 344-351, 2017.

[31] M. Obana, K. Prasad, A. Ito and S. Torizuka, "The Possible Role of Nano Sized Precipitates on the Mechanical Properties of Additively Manufactured in 718 Superalloy," *Materiald Science and Engineering A,* vol. 826, 2021.

[32] Texas State University, *MTS Standard Operating Procedure,* Texas State University, 2014.

[33] MTS, *Tensile Testing Basics,* MTS, 2021.

[34] Leica Microsystems , *Leica DVM 6 user manual,* Heerbrugg, Switzerland: Leica Microsystems, 2022.

[35] J. T. G. J. Rutherford, "Additive Manufacturing Independent Study," Wright State University, Dayton, Ohio, 2018.

[36] M. G, R. Cao, J. Chen, X. Guo and Y. Jiang, "Analytical Investigation of Grain Size Dependence of Microhardness in High Nickel- Containing Reheated Weld Metal," *Archives of Civil and Mechanical Engineering,* vol. 17, pp. 935-942, 2017.

[37] G. F. V. Voort and G. M. Lucas, "Microindentation Hardness Testing," *Advanced Materials and Processes,* pp. 21-25, 2018.

[38] Buehler, *Wilson Diamet User Guide,* Lake Bluff, Illinois: Buehler, 2016.

[39] C. Snyder, S. Attanasio and T. White, "Fatigue and Mechanical Properties of Laser Powder Bed Fusion 316L Stainless Steel," in *TMS2020 149th Annual Meeting and Exhibition*, 2020.

[40] B. Yang and F.-Z. Xuan, "Nonhomogenous Microstructure Related Creep Damage of the CrMoV Multi-pass Weld Metal," *Materials Science and Engineering,* vol. A, no. 763, 2019.

[41] W. Callister, Materials science and Engineering: an Introduction, New York, NY: J. Wiley, 2003.

[42] W. F. Hostford, Mechanical Behavior of Materials 2nd edition, Cambridge University Press, 2009.

[43] Y. Tian, D. Mcallister, H. Colijn, M. Mills, D. Farson, M. Nordin and S. Babu, "Rationalization of microstructure heterogeneity in inconel 718 builds made by the direct laser additive manufacturing process," *Metall. Mater. Trans. ,* vol. A 45, no. 10, pp. 4470-4483, 2014.

[44] Q. L. Zhang, J. H. Yao and J. Mazumder, "Laser Direct Metal Deposition Technology and Microstructure and Composition Segragation of INCONEL 718 Superalloy," *J. Iron Steel. Res. Int.,* vol. 18, no. 4, pp. 73-78, 2011.

Appendix A Microhardness line tests

The following are all the graphs for the microhardness line tests.

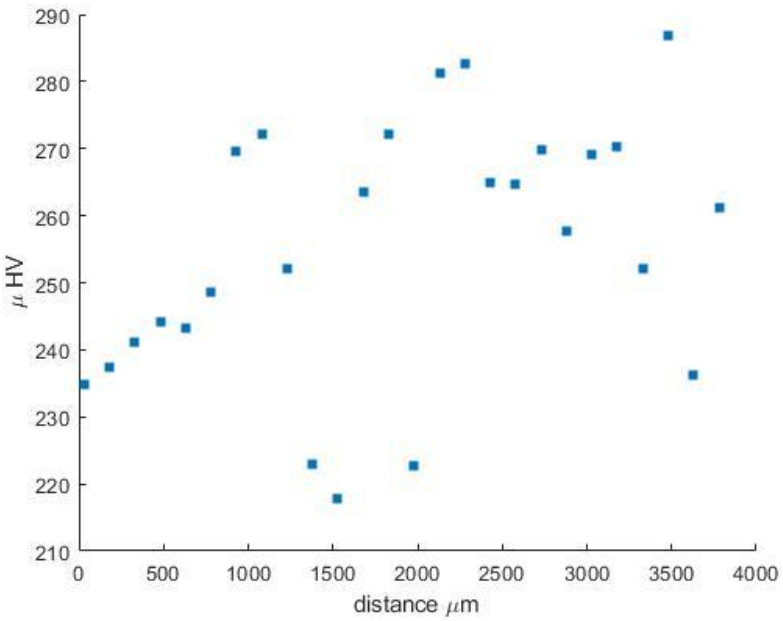

Figure 32: Graph of line test 1 for sample fabricated with 230 W, 4 mm diameter and in the XY plane.

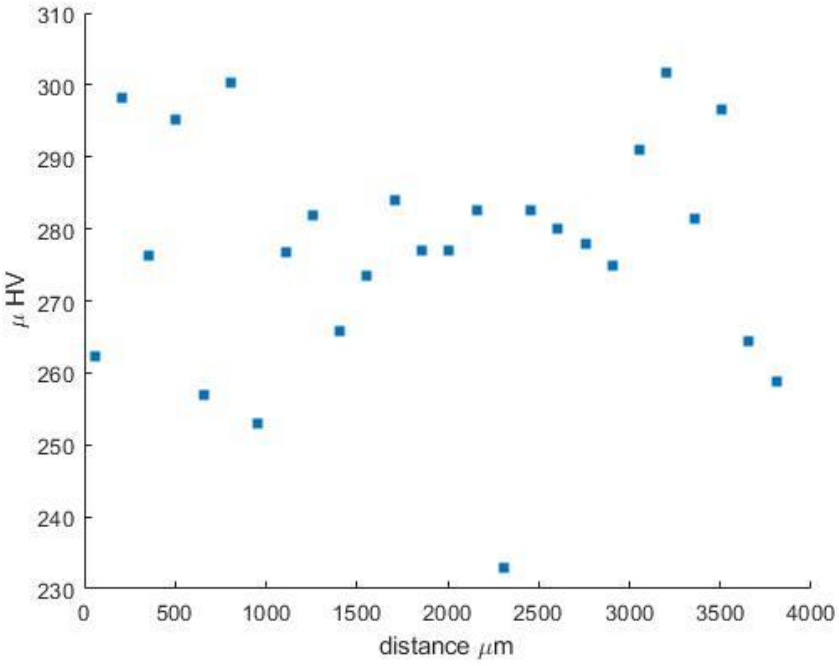

Figure 33: Graph of second line test for sample fabricated with 230 W, diameter of 4 mm and in the XY plane.

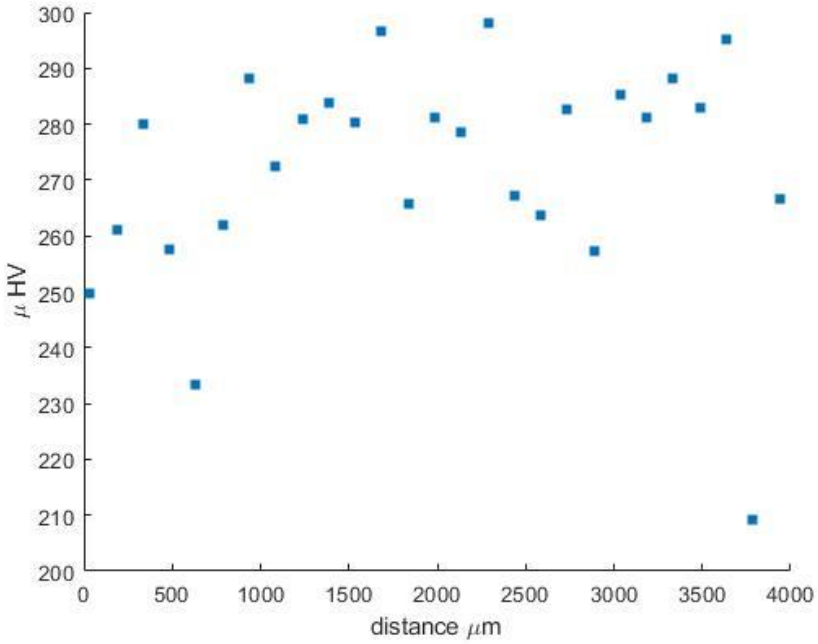

Figure 34: Graph of third line test for sample fabricated with 230 W, 4 mm diameter, and taken in XY plane.

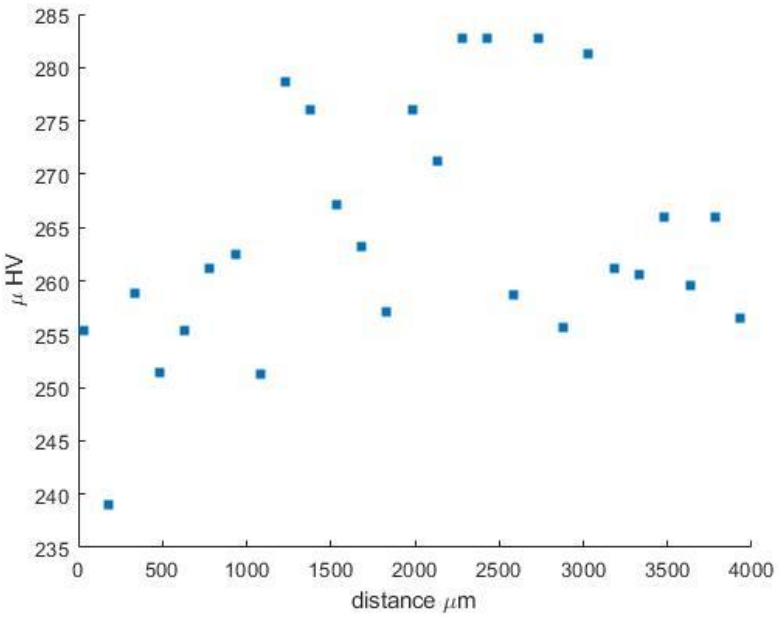

Figure 35: graph of line test 1 for sample fabricated using 230 W, 4 mm diameter, and taken in the YZ plane.

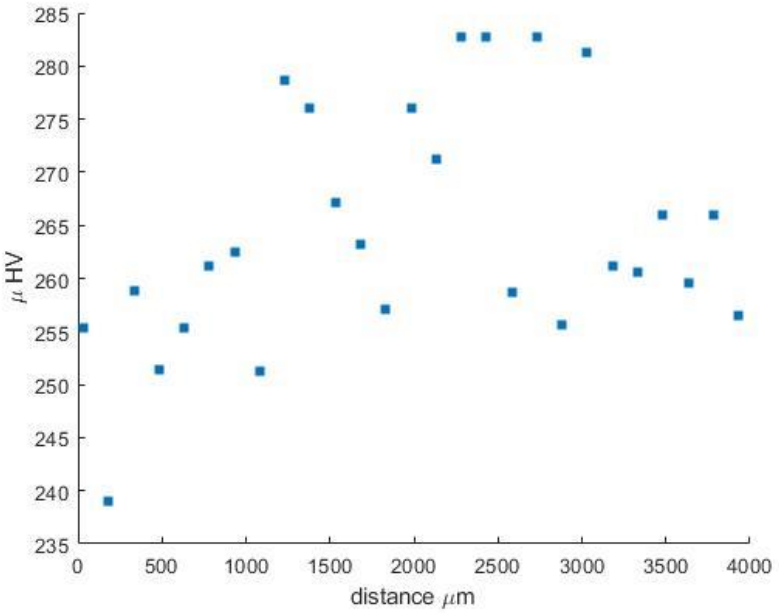

Figure 36: Graph of line test 2 for sample fabricated with 230 W, 4 mm, and taken in YZ plane.

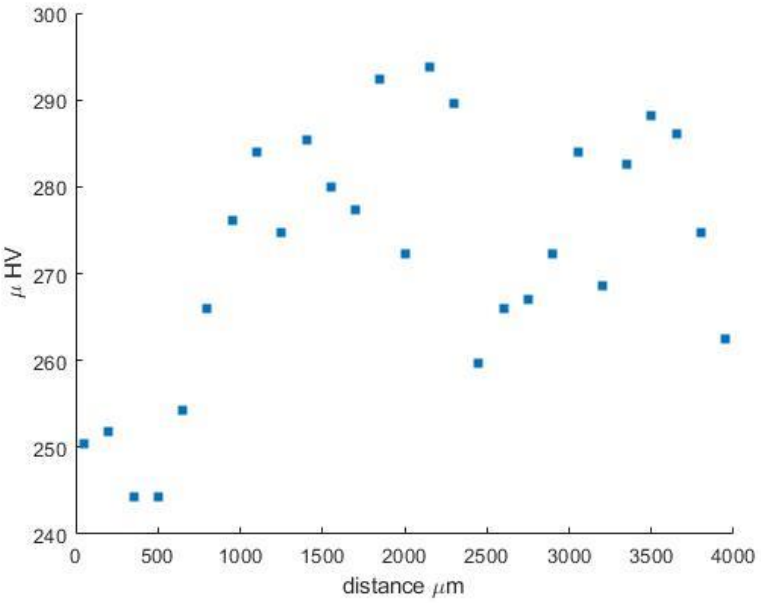

Figure 37: Graph of line test 3 fabricated with 230 W, 4 mm diameter, and taken in the YZ plane.

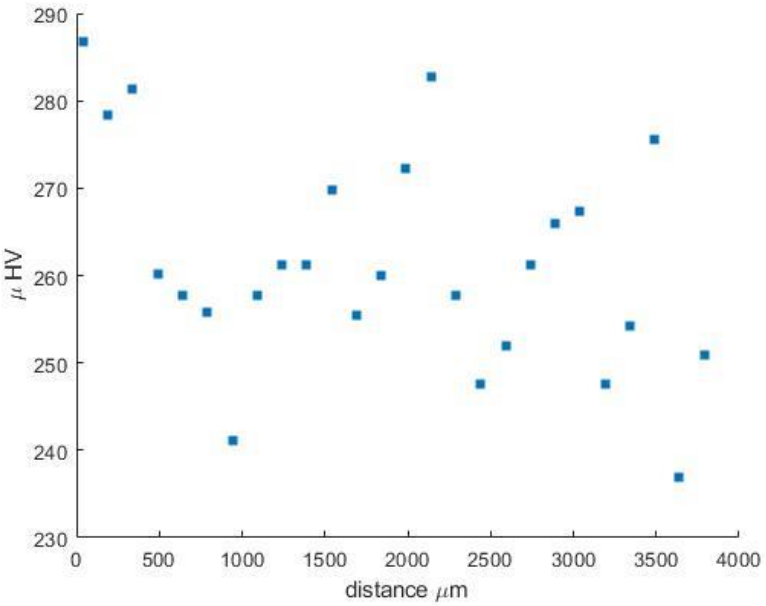

Figure 38: Graph of line test 1 for sample fabricated with 330 W, 4 mm Diameter, and taken in the XY plane.

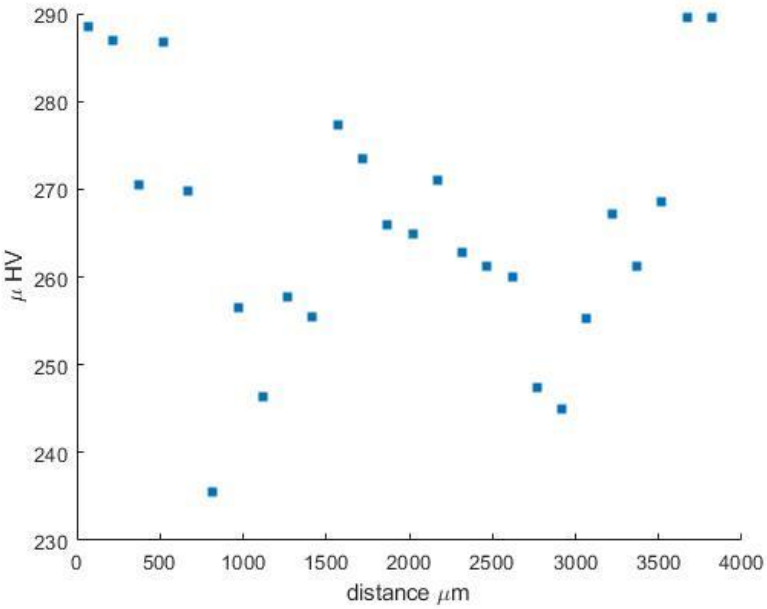

Figure 39: Graph of line test 2 for sample fabricated with 330 W, 4 mm diameter, and taken in the XY plane.

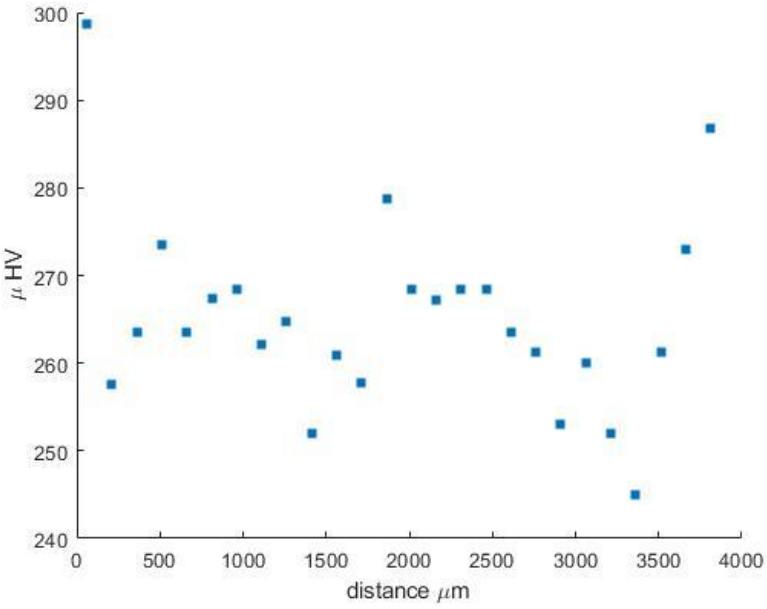

Figure 40: Graph of line test 3 for sample fabricated with 330 W, diameter of 4 mm, and taken in the XY plane.

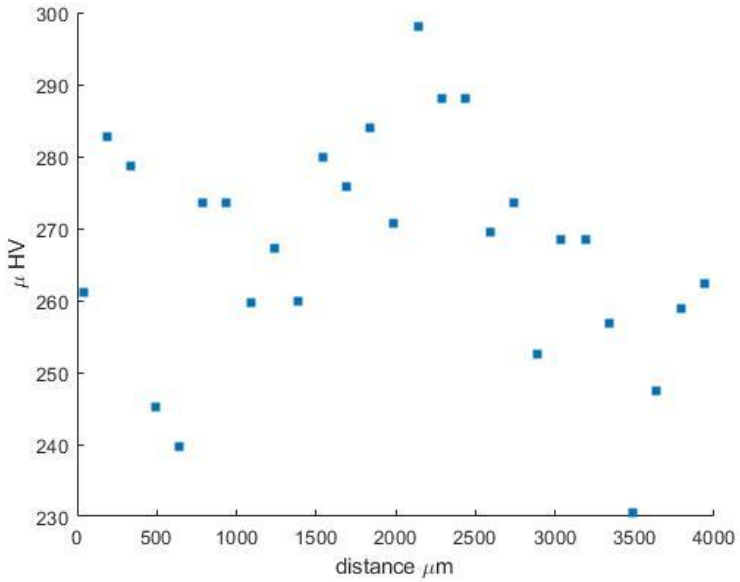

Figure 41: Graph of line test 1 for sample fabricated with 330 W, diameter of 4 mm, and taken in the YZ plane.

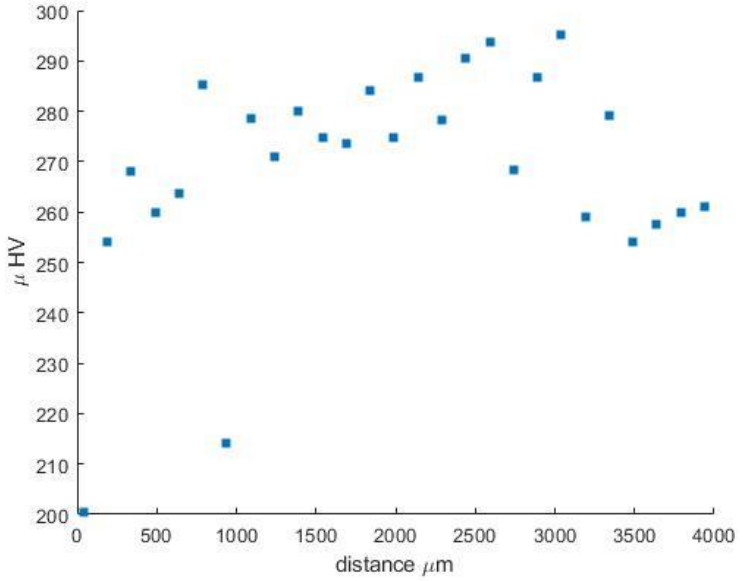

Figure 42: Graph of line test 2 for sample fabricated with 330 W, diameter of 4 mm, and taken in the YZ plane.

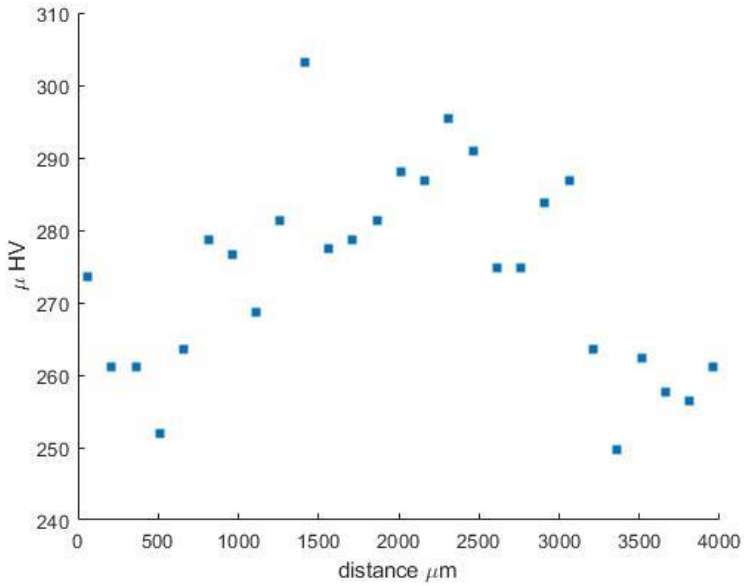

Figure 43: Graph of line test 3 for sample fabricated with 330 W, diameter of 4 mm, and taken in the YZ plane.

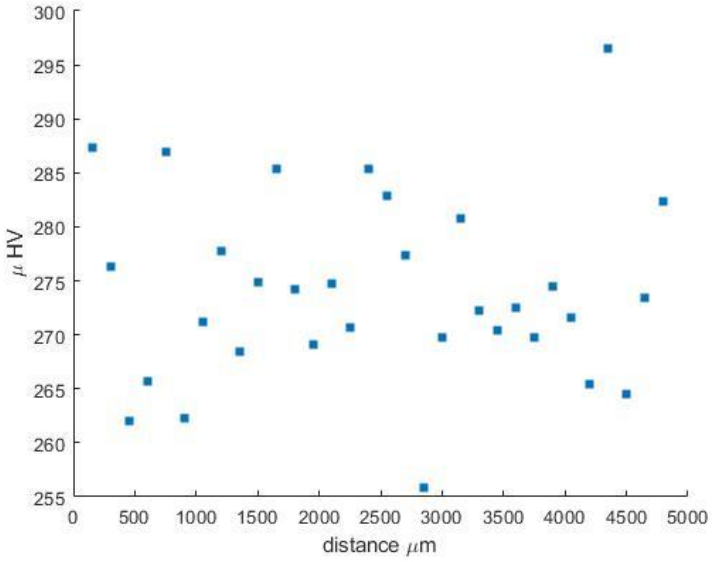

Figure 44: Graph of line test 1 for sample fabricated with 230 W, diameter of 5 mm, and taken in the XY plane.

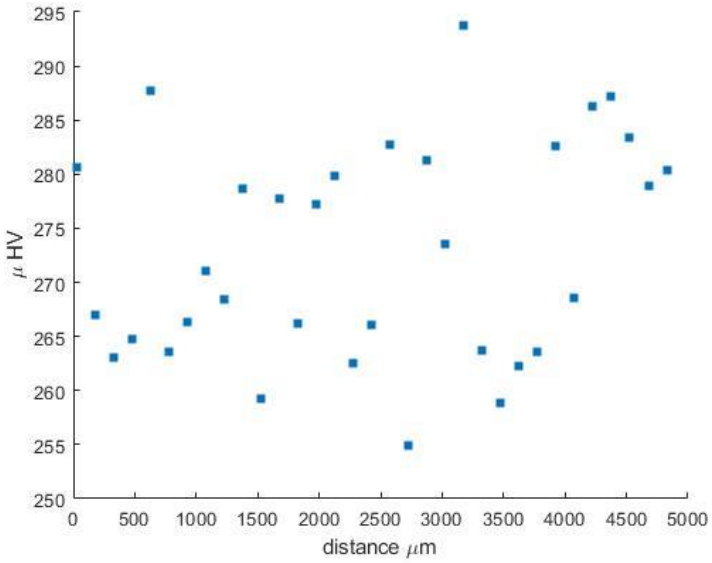

Figure 45: Graph of line test 2 for sample fabricated with 230 W, diameter of 5 mm, and taken in the XY plane.

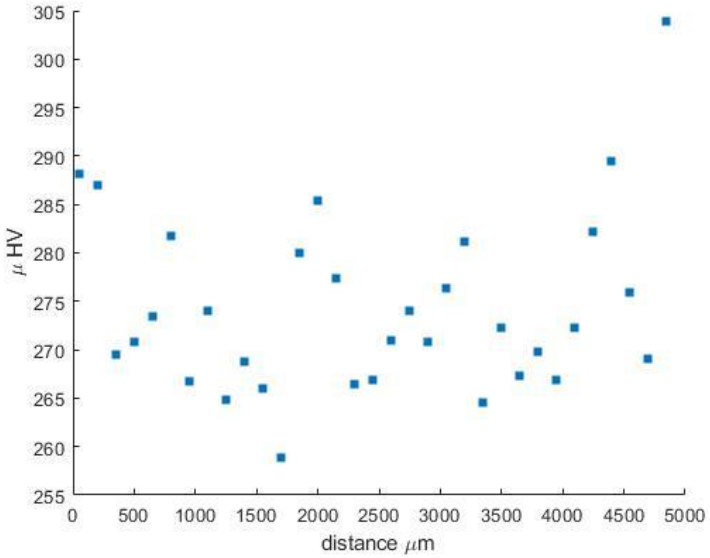

Figure 46: Graph of line test 3 for sample fabricated with 230 W, 5 mm diameter, and taken in the XY plane.

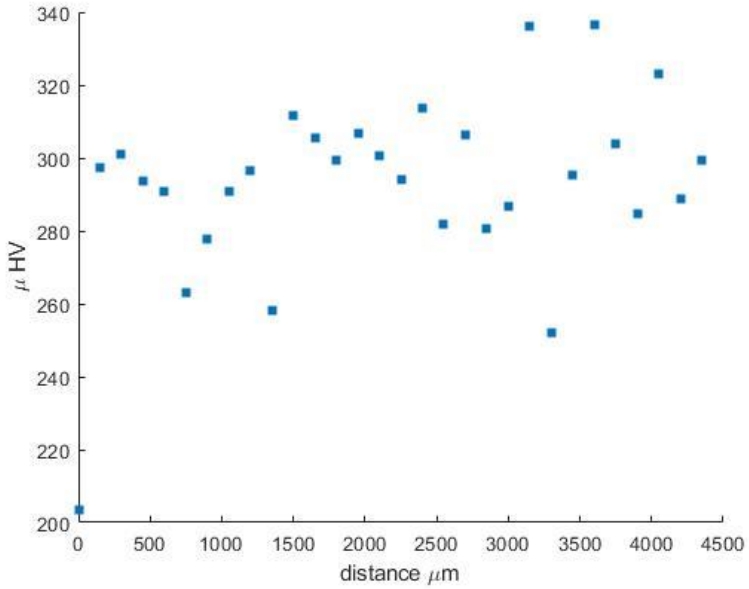

Figure 47: Graph of line test 1 from sample fabricated with 330 W, a diameter of 5 mm, and taken on the YZ plane.

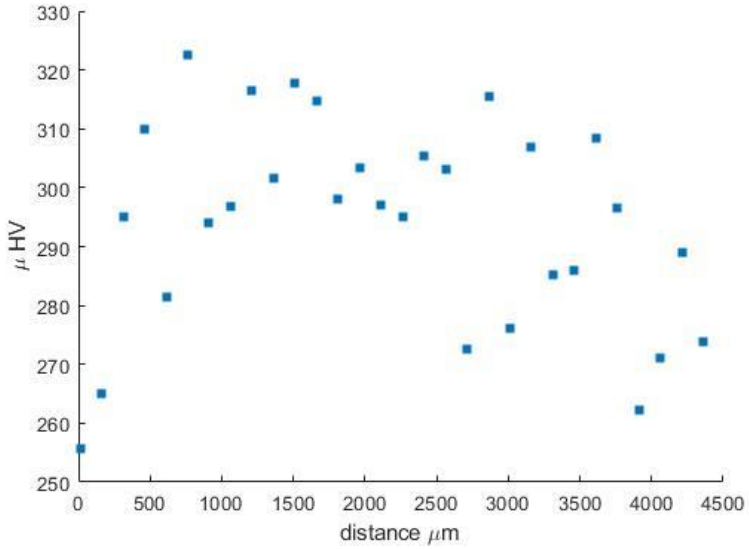

Figure 48: Graph of line test 2 from a sample fabricated with 330 W, a diameter of 5 mm, and taken on the YZ plane.

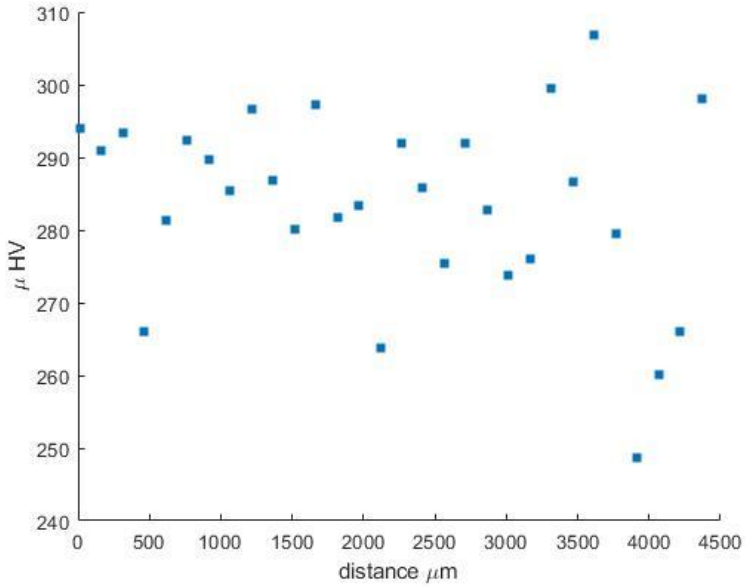

Figure 49: Graph of line test 3 from a sample fabricated with 330 W, a diameter of 5 mm, and taken in the YZ plane.

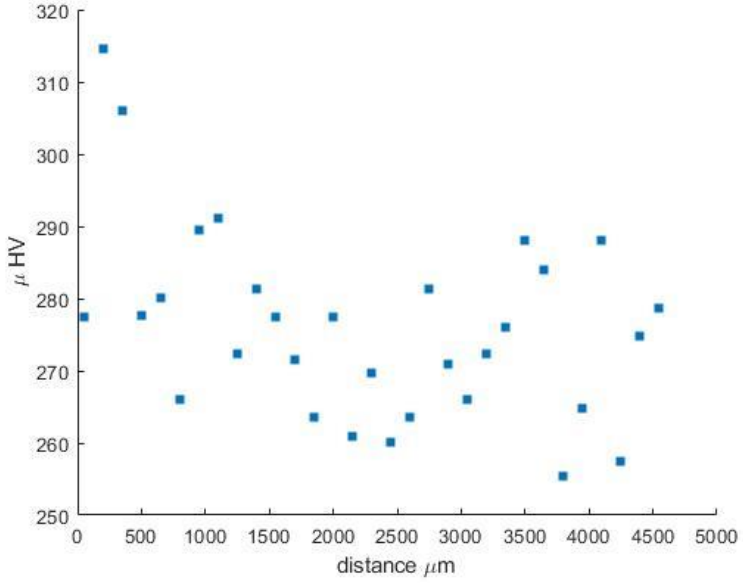

Figure 50: Graph of line test 1 from sample fabricated with 280 W, a diameter of 5 mm, and taken on the XY plane.

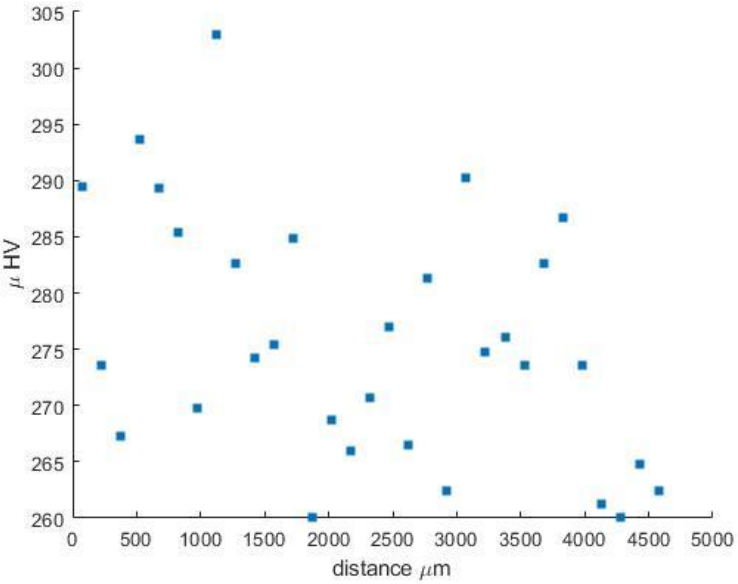

Figure 51:Graph of line test 2 for sample fabricated with 280 W, a diameter of 5 mm, and taken on the XY plane.

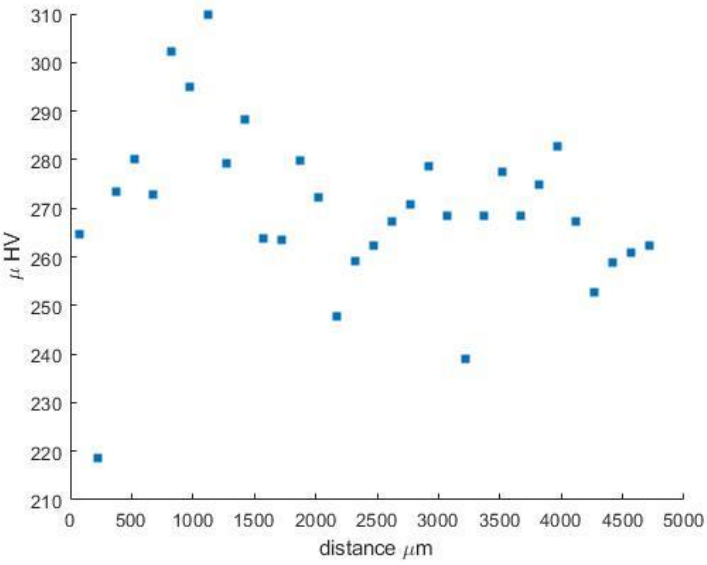

Figure 52:Graph of line test 3 for sample fabricated with 280 W, a diameter of 5 mm, and taken on the XY plane.

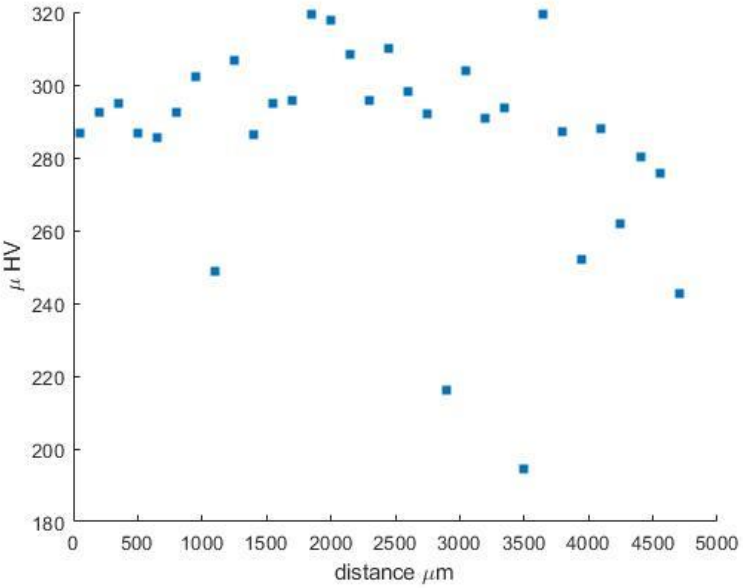

Figure 53: Graph of line test 1 for sample fabricated with 280 W and a diameter of 5 mm and taken on YZ plane.

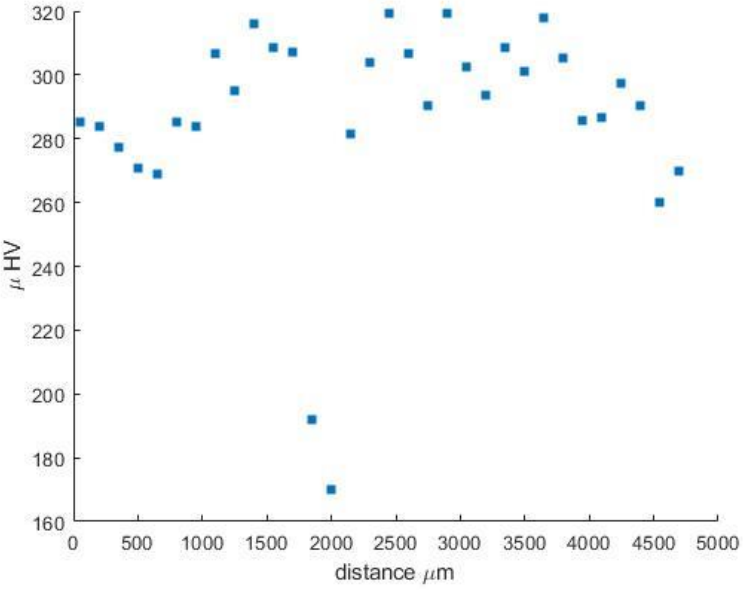

Figure 54: Graph of line test 2 for sample fabricated with 280 W, a diameter of 5 mm, and taken in YZ plane.

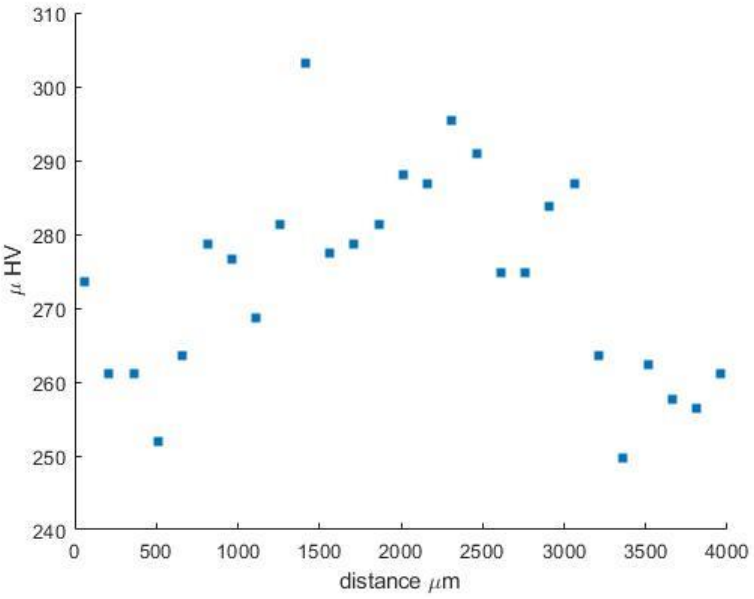

Figure 55: Graph of line test 3 for sample fabricated with 280 W, a diameter of 5 mm, and taken in the YZ plane.

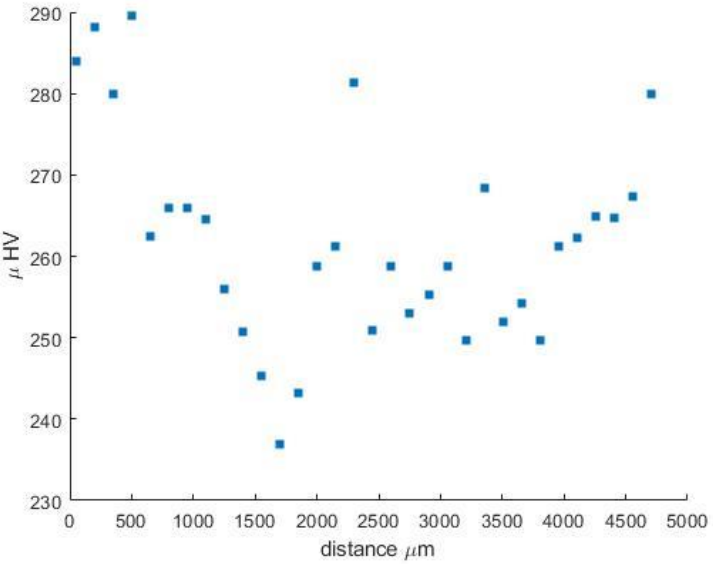

Figure 56: Graph of line test 1 for sample fabricated with 330 W, with a diameter of 5 mm, and taken in the XY plane.

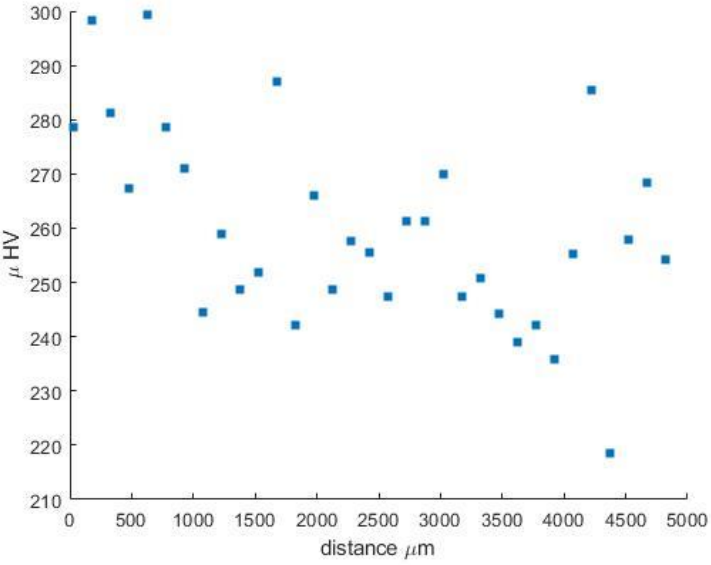

Figure 57: Graph of line test 2 from sample fabricated with 330 W, a diameter of 5 mm and taken from the XY plane.

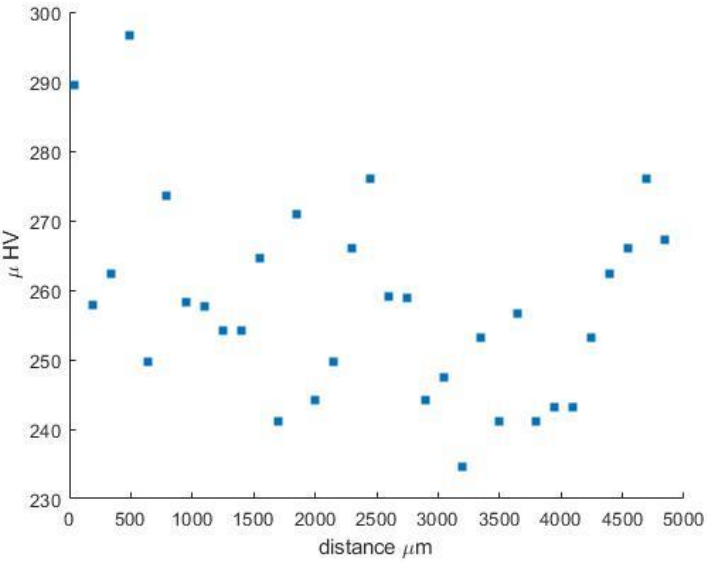

Figure 58: Graph of line test 3 from sample fabricated with 330 W, a diameter of 5 mm, and taken from the XY plane.

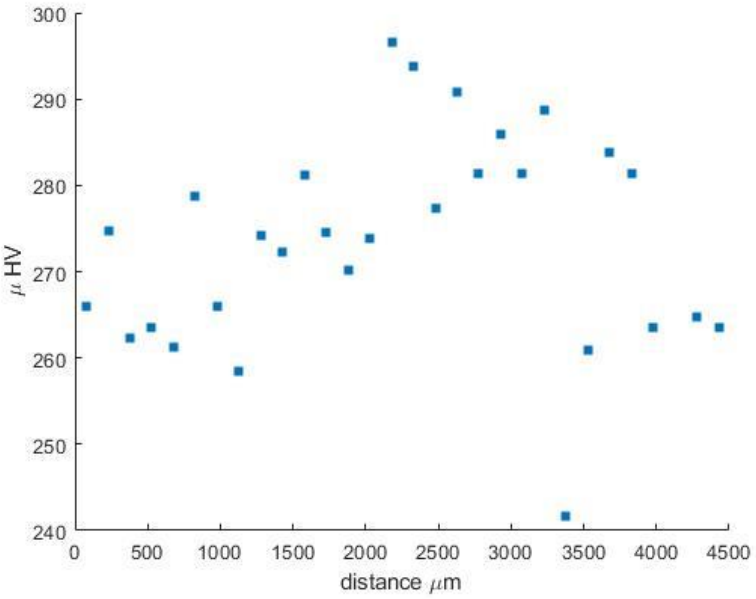

Figure 59: Graph of line test 1 for sample fabricated with 330 W, a diameter of 5 mm, and taken on the YZ plane.

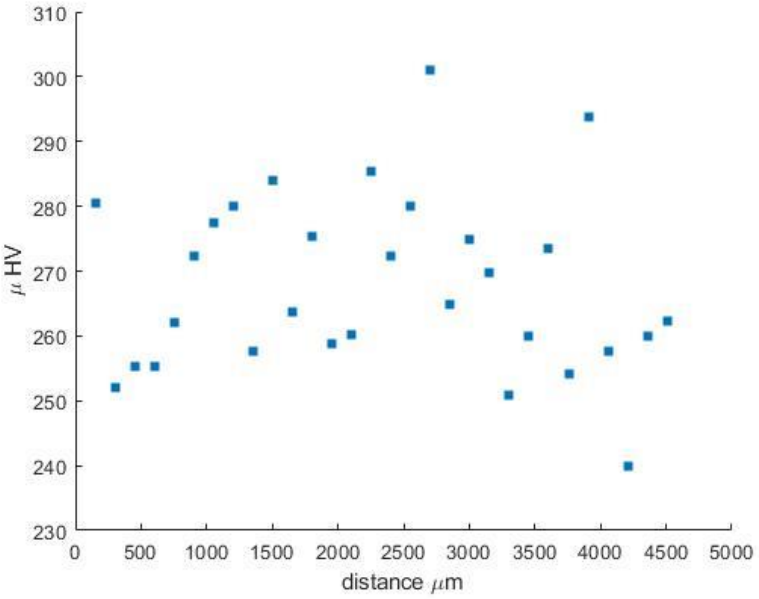

Figure 60: Graph of line test 2 from sample fabricated with 330 W, a diameter of 5 mm, and taken on the YZ plane.

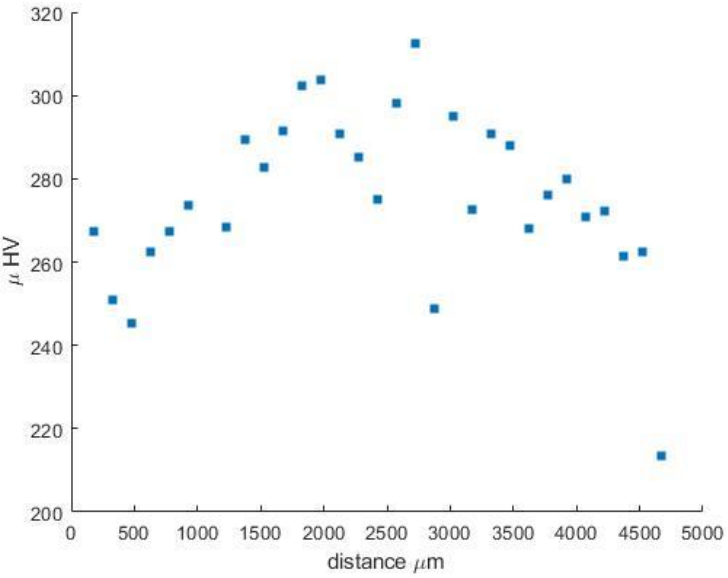

Figure 61: Graph of line test 3 from sample fabricated with 330 W, a diameter of 5 mm, and taken in the YZ plane.

Appendix B Fractography Images

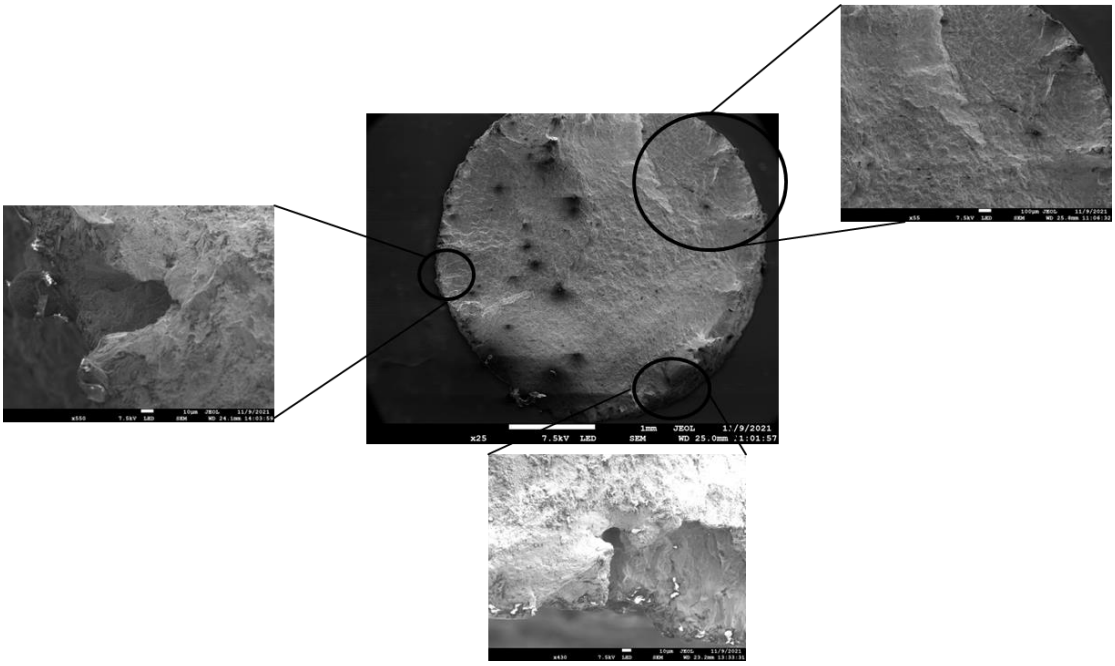

Figure 62: Fractography of fatigue sample 1 fabricated with 230 W

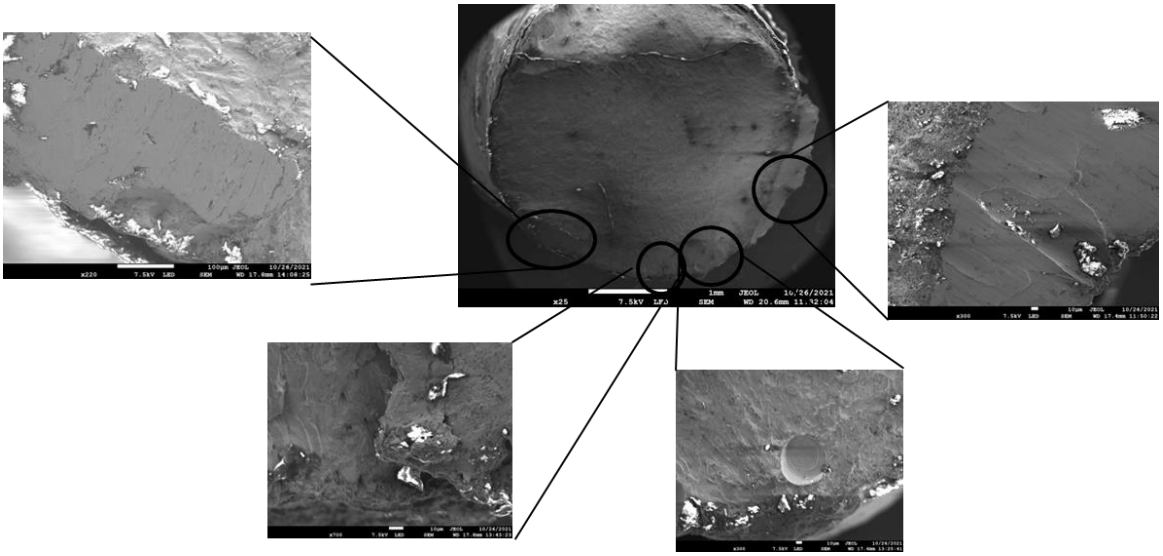

Figure 63: Fractography of fatigue bar 2 fabricated with 230 W.

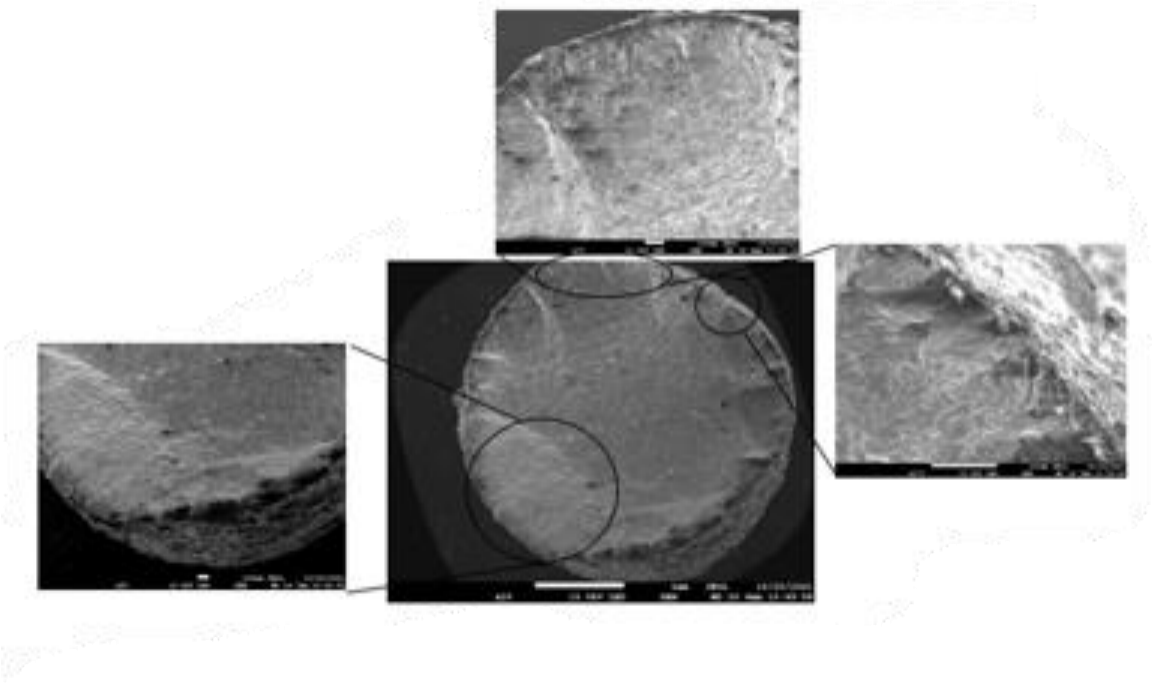

Figure 64: Fractography of fatigue sample 3 fabricated with 230 W.

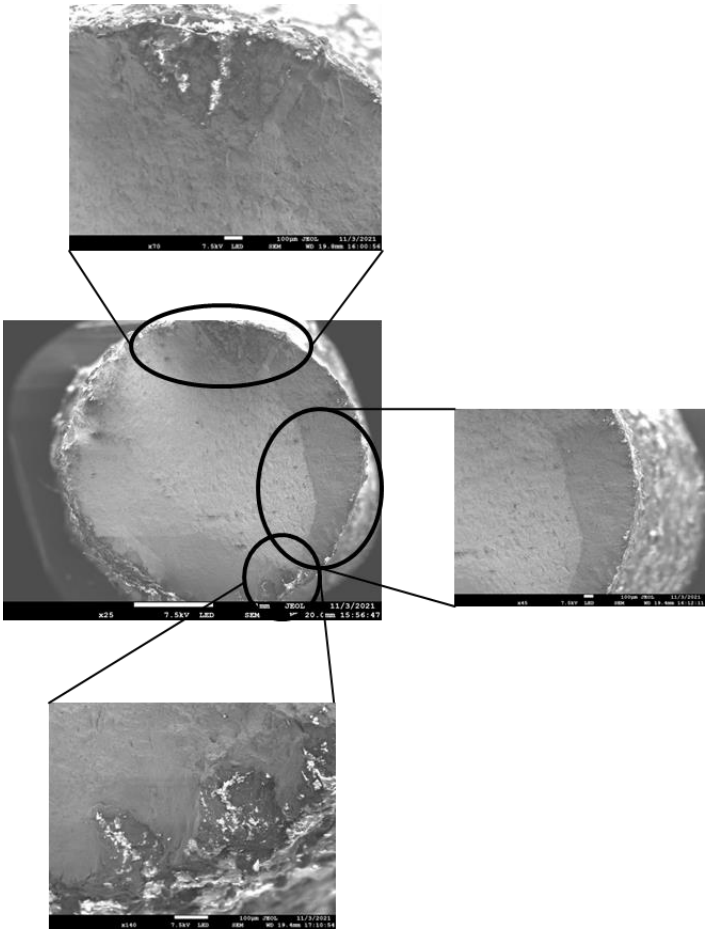

Figure 65: Fractography of fatigue sample 1 fabricated with 280 W.

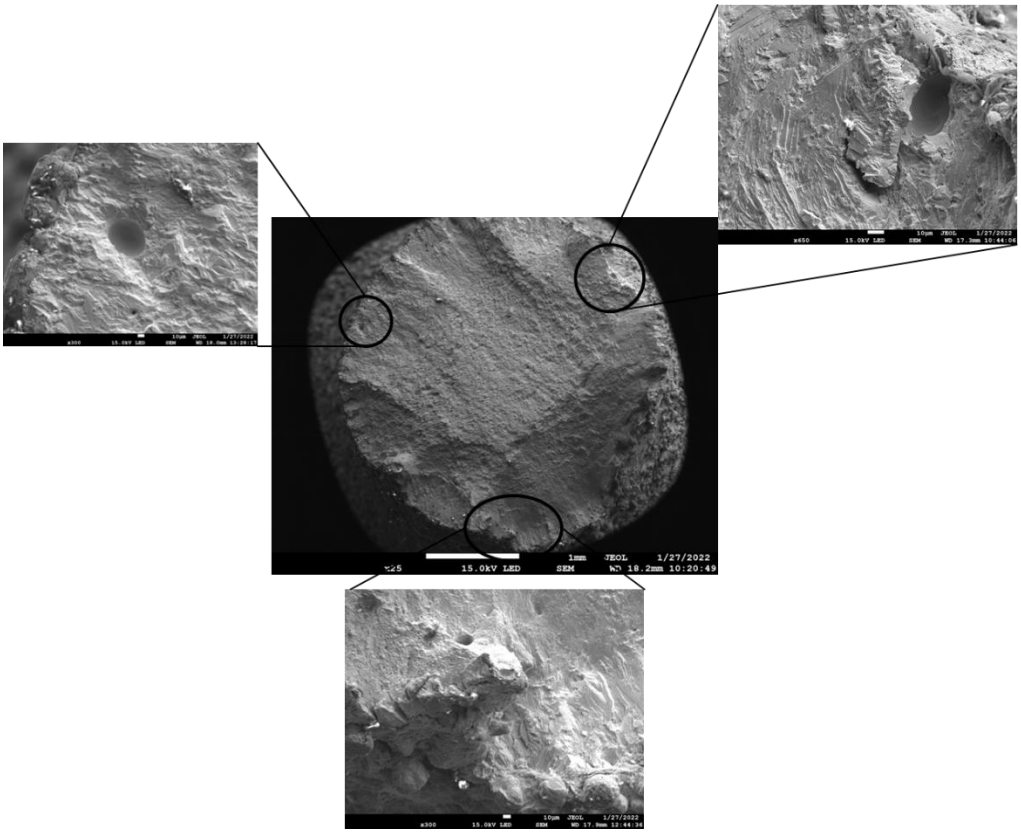

Figure 66: Fractography of fatigue sample 2 fabricated with 280 W.

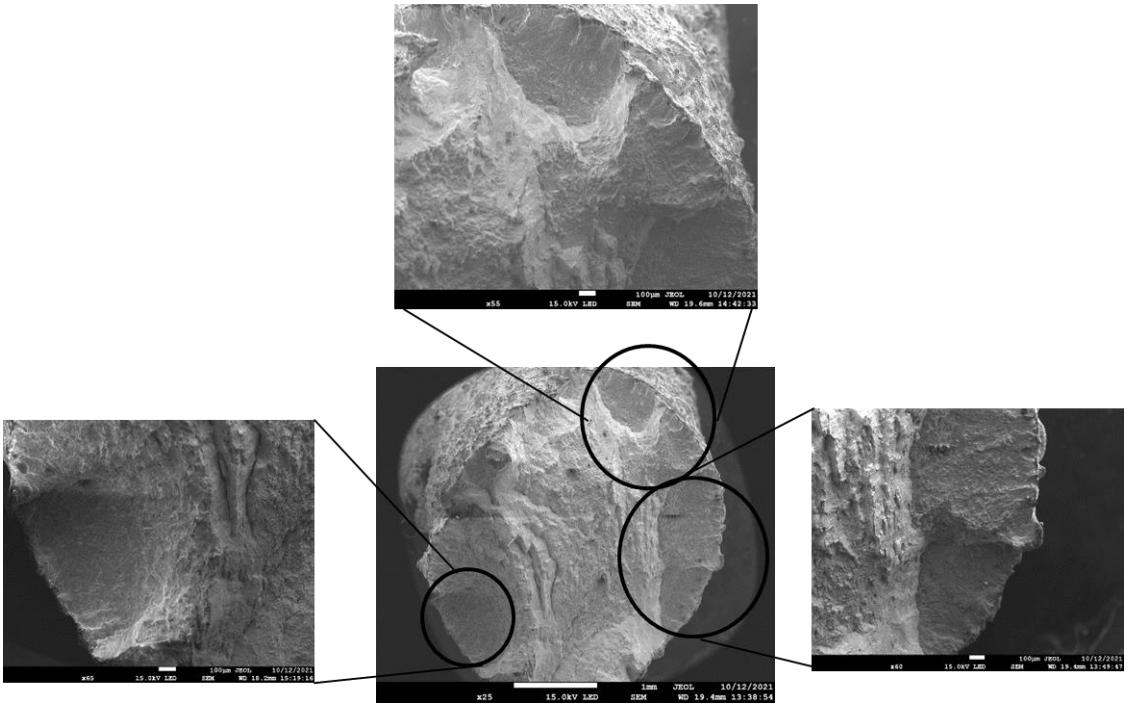

Figure 67: Fractography for fatigue sample 3 fabricated with 280 W.

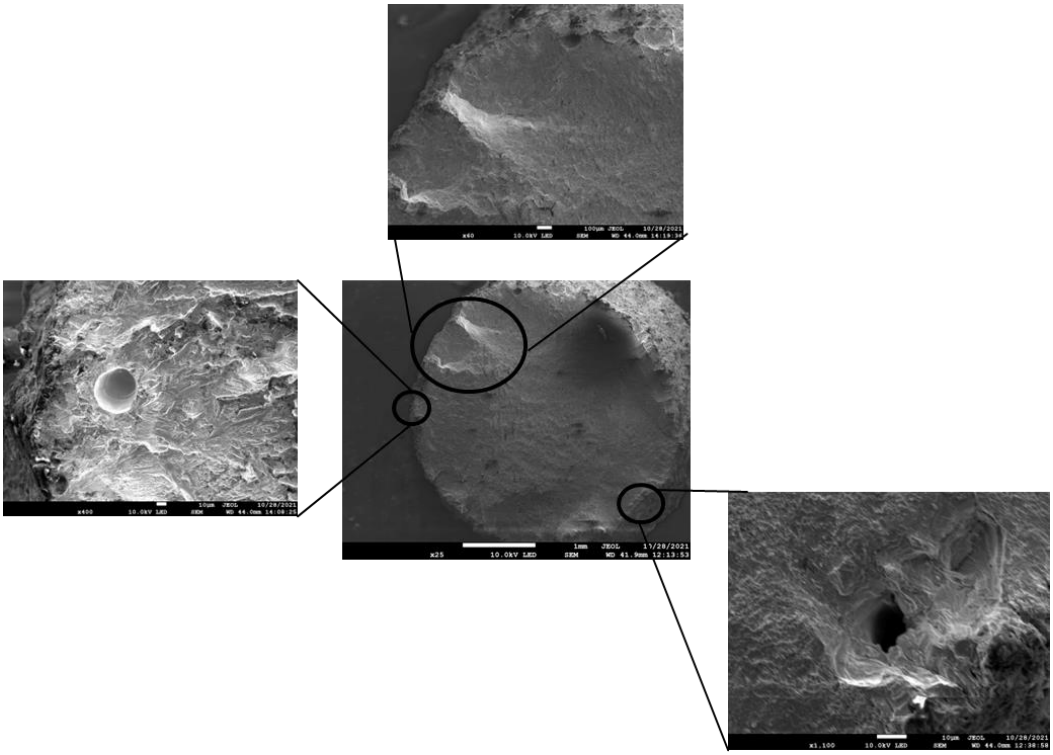

Figure 68: Fractography of fatigue sample 1 fabricated with 330 W.

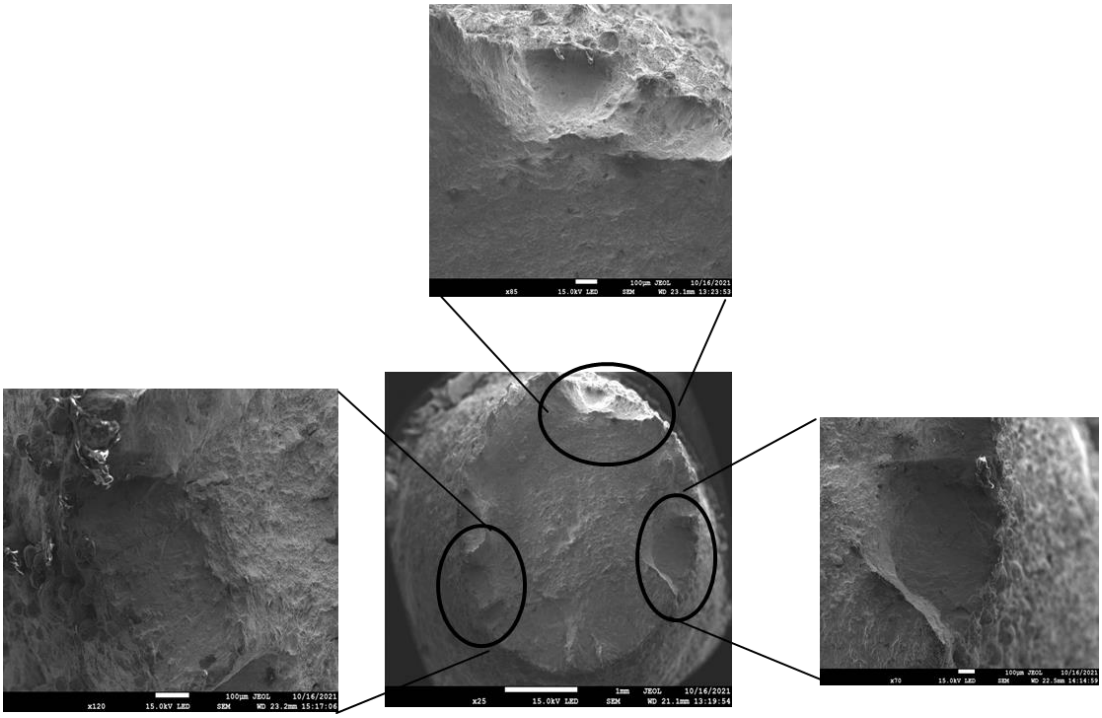

Figure 69: Fractography from fatigue sample 2 fabricated with 330 W.

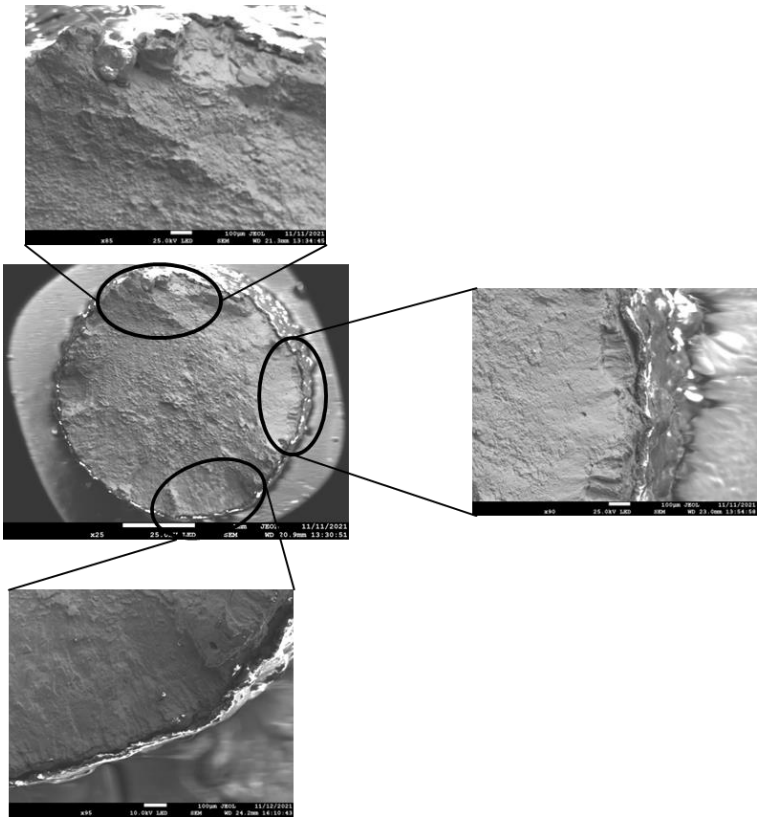

Figure 70: Fractography of sample 3 fabricated with 330 W.

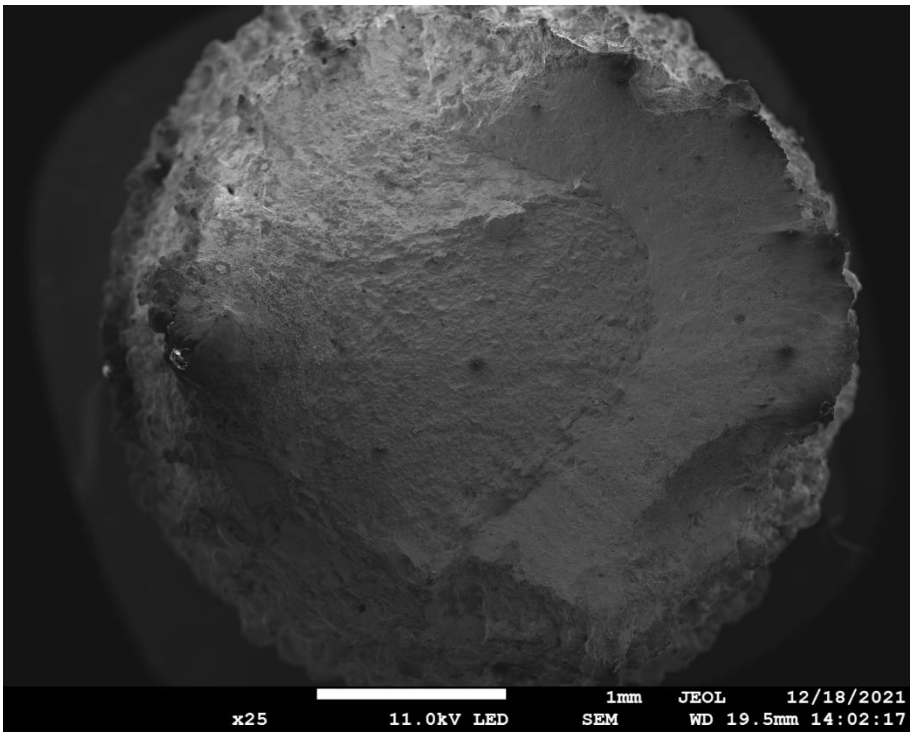

Figure 71: Fractography for 230 W tensile sample

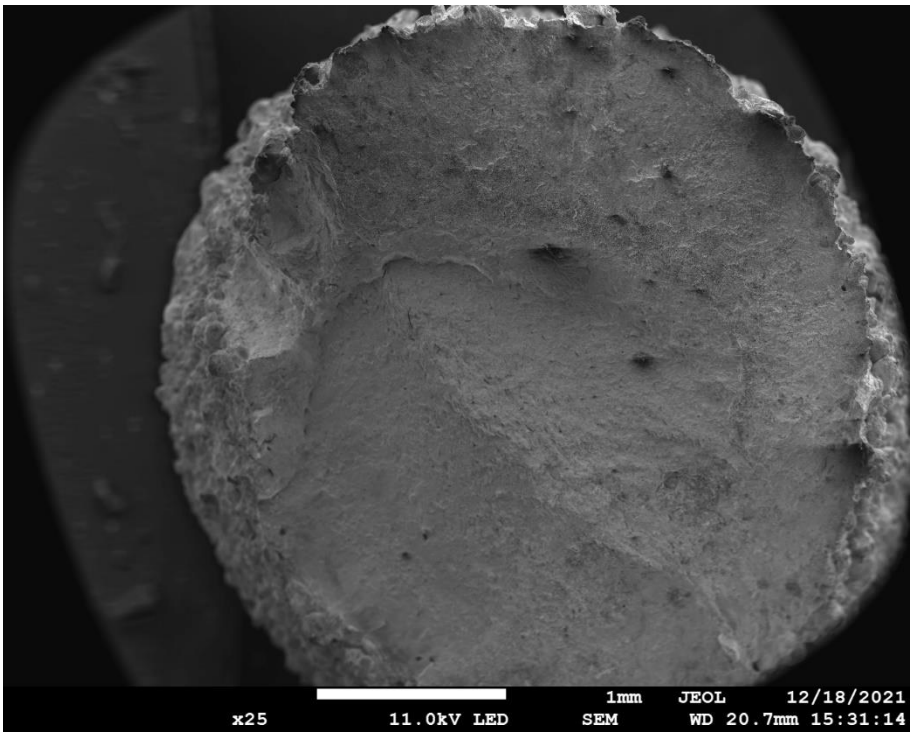

Figure 72: Fractography for 280 W tensile sample.

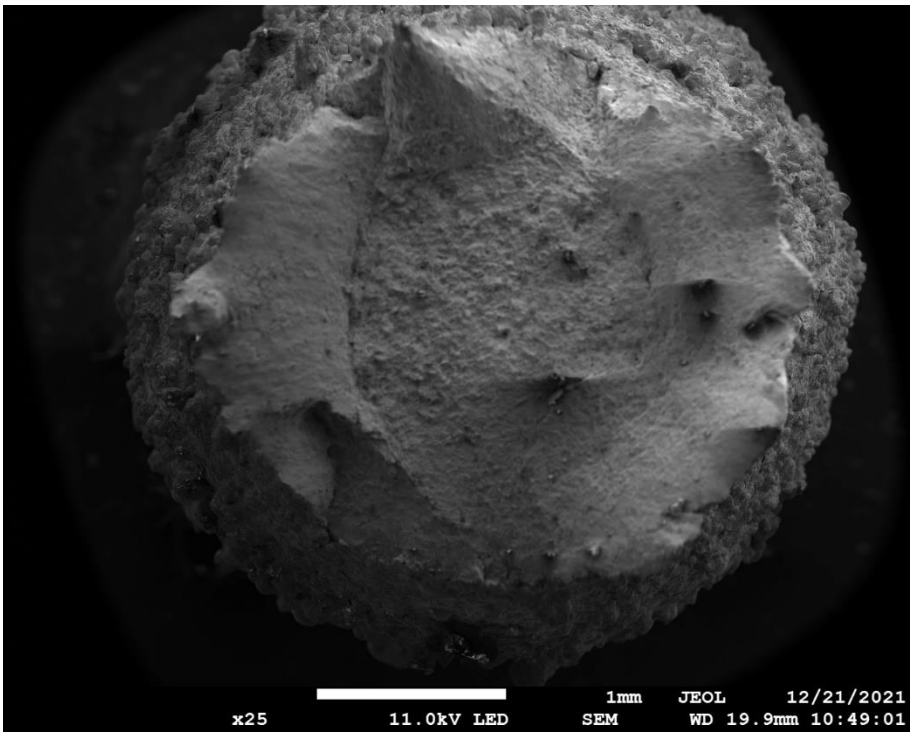

Figure 73: fractography image for 330W tensile sample